Paper No.
05556

CORROSION 2005

A MULTIPHASE FLOW AND INTERNAL CORROSION PREDICTION MODEL FOR MILD STEEL PIPELINES

Srdjan Nešić, Jiyong Cai and **Kun-Lin John Lee**
Institute for Corrosion and Multiphase Technology
Ohio University
342 W. State St, Athens, OH 45701 U.S.A

ABSTRACT

A number of CO_2 corrosion models can predict successfully the "worst case" corrosion rate but fail when more complex effects need to be included such as protective scale formation, water entrainment/wetting and the H_2S effect. A comprehensive integrated CO_2 / H_2S corrosion – multiphase flow model package has been built that takes into account the effect of most important variables and processes in internal pipeline corrosion including the effects of H_2S, water entrainment in multiphase flow, corrosion inhibition by crude oil components and localized attack.

In the text below it is described how the model can account for formation of iron carbonate and iron sulfide scales and predict their morphology as well as the effect on the corrosion rate. It is then shown how the model can successfully predict the critical velocity for entraining free water by the flowing oil phase as well as the effect of the key variables. The model has been extensively calibrated with laboratory data and compared with limited field data.

Keywords: CO_2 / H_2S corrosion, water entrainment, water wetting, model, prediction

INTRODUCTION

A variety of models for internal corrosion of mild steel oil and gas pipelines carrying multiphase flow (mixture of oil, gas and water) has appeared over the past thirty years following the pioneering attempts of deWaard and Milliams[1] in 1973. In a 2002 paper, Nyborg[2] reviewed the performance of a representative group of models concluding that most of the models predict successfully the "worst case" CO_2 corrosion rate but vary widely when more complex effects are included (e.g. protective scales, water entrainment/wetting, H_2S, etc). The main reason for this spread lies in the arbitrary nature of the

empirical correction factors that are employed to account for the various complicating effects. That review did not include the recently released MULTICORP V3.0 package from Ohio University (referred to as "model" in the text below). The outline of this integrated CO_2 corrosion – multiphase flow modeling package has been presented in a 2003 paper by Nesic et al.[3] The model takes into account the effect of most important variables and processes such as:

- Kinetics of electrochemical reactions at the steel surface.
- Transient one-dimensional transport of species between the bulk solution and the steel surface, through the turbulent boundary layer and through a porous surface scales.
- Kinetics of chemical reactions including precipitation.
- Kinetics of scales growth and the effect on corrosion.
- Effect of multiphase flow.
- Effect of H_2S.
- Effect of steel type.
- Effect of inhibition by crude oil and/or corrosion inhibitors.
- Localized attack.

The model is mechanistic in nature, fully transparent and resides on solid theoretical background. The foundation of the model is a large laboratory database on corrosion in multiphase flow. Since the majority of the features for this model and its verification have been presented in the NACE 2004 paper[3] the present paper will focus on a few key issues which Nyborg's review[2] has identified as most significant challenges in internal pipeline corrosion modelling for the future.

- Effect of H_2S on the growth and protectiveness of iron sulfide scales.
- Effect of multiphase flow on internal pipeline corrosion with a focus on modeling of entrainment and separation in oil/water two-phase flow.

Some of the other new developments included in this model are concurrently presented in separate papers at the same NACE 05 conference: by Hernandez et al.[4] (corrosion inhibition by crude oil components), Xiao and Nesic[5] (localized corrosion), Lee and Nesic[6] (effect of H_2S in the absence of sulfide scales).

EFFECT OF H_2S ON GROWTH AND PROTECTIVENESS OF IRON SULFIDE SCALES

The Background Model of CO_2 Corrosion

At the heart of this corrosion model are the theoretical equations that describe the most of the important processes present in uniform CO_2 corrosion of carbon steel, as listed above. The physical, mathematical and numerical aspects of the model were explained in detail in the past publications[7-9], however a brief outline is given below to facilitate the understanding of the new developments in the model.

The corrosion model is built around a mass transfer model that describes the movement of the species involved in the corrosion process between the metal surface and the bulk fluid. Since it describes uniform corrosion, a one-dimensional computational domain is used, stretching from the steel surface

through the pores of a surface scale and the mass transfer boundary layer, ending in the turbulent bulk of the solution. The concentration of each species is governed by a species conservation (mass balance) equation. A universal form of the equation which describes transport for species *j* in the presence of chemical reactions, which is valid both for the liquid boundary layer and the porous scale, is:

$$\underbrace{\frac{\partial(\varepsilon c_j)}{\partial t}}_{\text{accumulation}} = \underbrace{\frac{\partial}{\partial x}\left(\varepsilon^{1.5} D_j^{eff} \frac{\partial c_j}{\partial x}\right)}_{\text{net flux}} + \underbrace{\varepsilon R_j}_{\substack{\text{source or sink} \\ \text{due to chemical reactions}}} \tag{1}$$

where c_j is the concentration of species *j* in *kmol* m^{-3}, ε is the porosity of the scale, D_j^{eff} is the effective diffusion coefficient of species *j* (which includes both the molecular and the turbulent component) in m^2 s^{-1}, R_j is the source or sink of species *j* due to all the chemical reactions in which the particular species is involved in *kmol* $m^{-3}s^{-1}$, *t* is time and *x* is the spatial coordinate in *m*. It should be noted that in the transport equation above electromigration has been neglected as its contribution to the overall flux of species is small when it comes to spontaneous corrosion. Turbulent convection has been replaced by *turbulent diffusion* as the former is difficult to determine explicitly in turbulent flow. A well-established statistical technique is used here: instantaneous velocity is divided into the steady and the turbulent - fluctuating components. Close to a solid surface, the steady velocity component is parallel to the surface and does not contribute to the transport of species in the direction normal to the metal surface. The turbulent convection term can be approximated by a "turbulent diffusivity" term[10], $-D_t \partial c_j / \partial x$ and lumped with the molecular viscosity term to give D_j^{eff}. The turbulent diffusion coefficient D_t, is a function of the distance from the metal or solid scale surface and is given by[10]:

$$D_t = \begin{cases} 0 & \text{for } x < \delta_f \\ 0.18\left(\dfrac{x-\delta_f}{\delta-\delta_f}\right)^3 \dfrac{\mu}{\rho} & \text{for } x > \delta_f \end{cases} \tag{2}$$

Where δ_f is the thickness of the porous scale in *m*. The liquid boundary layer thickness δ in *m* is typically a function of the Reynolds number. For pipe flow it reads:[10]

$$\delta - \delta_f = 25 Re^{-7/8} d \tag{3}$$

where *d* is the hydraulic diameter in *m*, $Re = \rho U d/\mu$ is the Reynolds number, *U* is bulk velocity in *m* s^{-1}, ρ is the density in *kg* m^{-3}, and μ is dynamic viscosity in *kg* m^{-2} s^{-1}. It is assumed that there is no fluid flow within the porous scale (for $x < \delta_f$).

When species *j* is involved *k* chemical reactions simultaneously, one can write for the source/sink term in (1):

$$R_j = a_{jk} r_k \tag{4}$$

where tensor notation applies for the subscripts, a_{jk} is the stoichiometric matrix where row *j* represents the *j*-th species, column *k* represents the *k*-th chemical reaction, and r_k is the reaction rate vector.

Chemical reactions of special interest are precipitation of iron carbonate and iron sulfide which have been implemented in the model as they take place at the steel surface and in the porous corrosion

scale. The precipitation reactions act as a sink for Fe^{2+}, CO_3^{2-}, S^{2-} ions, influencing the fluxes and concentration gradients for both the ions and all other carbonic and sulfide species. The kinetics of scale growth is described in more detail in the sections below.

One equation of the form (1) is written for each species. They all have to be solved simultaneously in space and time. The boundary conditions for this set of partial differential equations are: in the bulk - equilibrium concentrations of species (which is also used as the initial condition), and at the steel surface - a flux of species is determined from the rate of the electrochemical reactions (zero flux for non-electroactive species). This is where the link between corrosion and species transport is achieved. Corrosion determines the fluxes of the species at the metal surface and thus affects their transport into the solution, while in turn the transport rate and mechanisms affect the concentration of the species at the metal surface which determine the rate of corrosion. Hence a two-way coupling is achieved, what is physically realistic.

As the corrosion process is electrochemical in nature, the corrosion rate can be explicitly determined by calculating the rate of the electrochemical reactions underlying it such as: iron oxidation as well as reductions of hydrogen ion, carbonic, acetic acid, etc. The electrochemical reaction rate can be expressed as a current density, i (expressed in $A\ m^{-2}$), which is a function of the electrochemical potential at the metal surface, E (expressed in V):

$$i = \pm\, i_o \cdot 10^{\pm\frac{E-E_{rev}}{b}} \cdot \prod_{s=1}^{n_s}\left(1-\theta_s\right) \tag{5}$$

This equation is unique for each of the electrochemical reactions involved in a corrosion process such as hydrogen reduction, iron oxidation, etc. The "+" sign applies for anodic reactions while the "–" sign applies for cathodic reactions. θ_s is the fraction of the steel surface where a given electrochemical reaction does not occur because the surface is covered by a species s which could be an adsorbed inhibitor or a protective scale (such as iron carbonate or iron sulfide). The product sign $\prod$ accounts for a compounding (additive) effect by more than one surface species. For each electrochemical reaction, equation (5) is different because of the unique parameters defining it: i_o - the exchange current density in $A\ m^{-2}$, E_{rev} - the reversible potential in V, and b - the Tafel slope in V. These parameters have to be determined experimentally and are functions of temperature and in some cases species concentrations. An overview covering how these parameters are calculated in the present model is given elsewhere (reference[11] for the cathodic reaction and reference[12] for the anodic reaction). The unknown electrochemical potential at the metal surface E in (5), is also called corrosion potential or open circuit potential, which can be found from the current (charge) balance equation at the metal surface:

$$\sum_{a=1}^{n_a} i_a = \sum_{c=1}^{n_c} i_c \tag{6}$$

where n_a and n_c are the total number of anodic and cathodic reactions, respectively.

This brief introduction of the corrosion model brings us to the effect of H_2S. On one hand dissolved H_2S is a mild acid and can be treated as just another cathodic species given that the concentrations are high enough. However, the presence of H_2S can lead to formation of various forms of iron sulfide scales that can be either very protective or cause localized attack. In order to extend the mechanistic CO_2 corrosion model described above to cover the effect of H_2S, a systematic approach is taken here, where the complex effects of H_2S are introduced gradually. Firstly, it needs to be pointed out

that the focus of this paper is on rather small concentrations of H_2S (<350 ppm in the gas phase). Secondly, the effect of these trace amount of H_2S on CO_2 corrosion is initially described and modeled for low pH, deliberately avoiding the complex issues associated with precipitation of iron sulfide scales. The scales are introduced into the model subsequently. Therefore the following presentation about the effects of H_2S on CO_2 corrosion is done in two parts.

The Effect of H_2S

Recent experimental results[6] suggest that iron sulfide scales such as mackinawite can form on the surface of the steel via solid state reaction regardless of whether supersaturation with respect to iron sulfide is reached or not, which agrees with previous research done by Shoesmith et al.[13] These iron sulfide scales appear to have two distinct and opposite effects on corrosion: they inhibit the corrosion process (proportionally to surface coverage) what is dominant at very low H_2S concentrations, but also appear to have a corrosion accelerating effect at higher H_2S concentrations, probably by providing an increased surface area for the cathodic reaction. In order to account for these two effects, an equation including additive terms is proposed: a term representing a simple Langmuir-type H_2S adsorption isotherm (to account for the protection by mackinawite) is added to a term describing a first order catalytic effect (to account for the corrosion accelerating effect):

$$1-\theta_{H_2S} = \frac{1}{1+K_{a/d}\,c_{H_2S}} + k_c\,c_{H_2S} \tag{7}$$

where $K_{a/d}$ = the adsorption/desorption constant for H_2S and k_c is the catalytic rate constant. This model was verified by comparing the predictions with experimental results at low pH as illustrated in FIGURE 1.

The modelling of iron sulfide scale precipitation and growth and its complex interaction with CO_2/H_2S corrosion is discussed below. Using the iron carbonate scale growth model presented earlier[9] as a template, a similar methodology was followed to model the formation of iron sulfide scales due to the lack of quantitative information on iron sulfide formation, especially the kinetics of iron sulfide precipitation.

In CO_2 corrosion of carbon steel, when the concentrations of Fe^{2+} and CO_3^{2-} ions exceed the solubility limit, they can precipitate to form solid iron carbonate according to:

$$Fe^{2+} + CO_3^{2-} \rightarrow FeCO_{3(s)} \tag{8}$$

Similarly, in the presence of H_2S, when the concentrations of Fe^{2+} and S^{2-} ions exceed the solubility limit, they can precipitate to form solid iron sulfide according to:

$$Fe^{2+} + S^{2-} \rightarrow FeS_{(s)} \tag{9}$$

When scale precipitates at the steel surface, it can slow or stop the corrosion process by presenting a diffusion barrier for the species involved in the corrosion process. Scale growth depends primarily on the precipitation rate of either iron carbonate ($R_{FeCO_{3(s)}}$) or iron sulfide ($R_{FeS_{(s)}}$) or both. The scale grows in density as well as thickness as it precipitates. However, the steel surface corrodes under

the scale, continuously creating a "void" between the scale and the steel surface (here called "scale undermining"). As soon as it is created, the void starts filling by the ongoing precipitation.

The proposed equations describing the simultaneous iron carbonate and iron sulfide scale growth kinetics are obtained by writing mass balances (conservation equations) for the solid iron carbonate and iron sulfide:

$$\frac{\partial c_{FeCO_{3(s)}}}{\partial t} = R_{FeCO_{3(s)}} - CR\frac{\partial c_{FeCO_{3(s)}}}{\partial x} \tag{10}$$

$$\underbrace{\frac{\partial c_{FeS_{(s)}}}{\partial t}}_{\text{local change}} = \underbrace{R_{FeS_{(s)}}}_{\text{precipitation rate}} - \underbrace{CR\frac{\partial c_{FeS_{(s)}}}{\partial x}}_{\text{undermining rate}} \tag{11}$$

Since $FeCO_3$ and FeS are solids, its diffusion and convection can be neglected in above equation (10) and (11). The equations simply expresses the fact that the amount of solid iron carbonate $c_{FeCO_{3(s)}}$ or sulfide $c_{FeS_{(s)}}$ found in a given volume, (in *kmol* m^{-3}) will increase over time if there is precipitation (nonzero $R_{FeCO_{3(s)}}$ and/or $R_{FeS_{(s)}}$ in *kmol* m^{-3} s^{-1}) and will decrease due to the undermining effect, which is described by the last term on the right hand side in equation (10) and (11) as being proportional to the corrosion rate *CR*. The detailed explanations and the numerical treatment of these equations are described in the previous study.[9]

One convenient way to express the morphology of the scale is via the distribution of volumetric porosity ε since it is used as the principal scale parameter affecting transport of species (see equation 1). Volumetric porosity of the scale is defined as:

$$\varepsilon = \frac{V_{void}}{V_{total}} = 1 - \frac{V_{FeCO_{3(s)}}}{V_{total}} - \frac{V_{FeS_{(s)}}}{V_{total}} \tag{12}$$

where V_{total} is the total volume; $V_{FeCO_{3(s)}}$ is the part of that volume occupied by solid $FeCO_3$ and $V_{FeS_{(s)}}$ is the part of that volume occupied by solid FeS and V_{void} is the void (volume occupied by the solution), all in m^3. Rearranging and combining the scale growth equations (10) and (11) to express them in terms of porosity yields:

$$\frac{\partial \varepsilon}{\partial t} = -\frac{M_{FeCO_{3(s)}}}{\rho_{FeCO_{3(s)}}} R_{FeCO_{3(s)}} - \frac{M_{FeS_{(s)}}}{\rho_{FeS_{(s)}}} R_{FeS_{(s)}} - CR\frac{\partial \varepsilon}{\partial x} \tag{13}$$

where: $M_{FeCO_{3(s)}}$, $M_{FeS_{(s)}}$ are the molecular masses of $FeCO_3$ and FeS respectively, in *kmol* kg^{-1} and $\rho_{FeCO_{3(s)}}$, $\rho_{FeS_{(s)}}$ are the densities of $FeCO_3$ and FeS respectively, in *kg* m^{-3}.

The kinetics of iron carbonate scale formation $R_{FeCO_{3(s)}}$ is: [9-14]

$$R_{FeCO_{3(s)}} = K_{spFeCO_{3(s)}} \cdot e^{52.4 - \frac{119.8}{RT}} \cdot f\left(A/V\right) \cdot \left[S_{FeCO_{3(s)}} - 1 \right] \cdot \left[1 - \left(S_{FeCO_{3(s)}} \right)^{-1} \right] \quad (14)$$

where $K_{spFeCO_{3(s)}}$ is the solubility product for iron carbonate, the exponential term is an Arhenius-type function that accounts for temperature, $f\left(A/V\right)$ is a precipitation kinetics function that depends on the internal surface area of the scale, and $S_{FeCO_{3(s)}}$ is the solution supersaturation with respect to iron carbonate:

$$S_{FeCO_{3(s)}} = \frac{c_{Fe^{2+}} c_{CO_3^{2-}}}{K_{spFeCO_{3(s)}}} \quad (15)$$

Similarly the kinetics of iron sulfide precipitation $R_{FeS_{(s)}}$ in equation (13) can also be described as a function of the solubility product for iron sulfide, $K_{spFeS_{(s)}}$, solution supersaturation with respect to iron sulfide $S_{FeS_{(s)}}$:[15]

$$R_{FeS_{(s)}} = K_{spFeS_{(s)}} \cdot e^{16.2 - \frac{9520.6}{RT}} \cdot f\left(A/V\right) \cdot \left[\left(S_{FeS_{(s)}} \right)^{0.5} - 1 \right]^2 \quad (16)$$

where the solution supersaturation with respect to iron sulfide scale is:

$$S_{FeS_{(s)}} = \frac{c_{Fe^{2+}} c_{S^{2-}}}{K_{spFeS_{(s)}}} \quad (17)$$

Recently CO_2/H_2S corrosion experiments were conducted in supersaturated conditions in a high temperature, high pressure multiphase flow loop by Brown[16]. Experiments were conducted in a 1% NaCl solution at 60ºC, pH 6.0, 0.77 MPa partial pressure CO_2, with trace amounts of H_2S in both single phase flow (V= 1 m/s) and multiphase flow (V_{sg}=3 m/s, V_{sl}= 1 m/s). Corrosion testing was conducted in the region of low supersaturation values for iron carbonate ($S_{FeCO_{3(s)}}$ < 10) and three different supersaturation values for iron sulfide (2.5 < $S_{FeS_{(s)}}$ < 125) through adjustment of the partial pressure of H_2S for three 30 day exposures. Under the conditions tested, both iron carbonate and mackinawite scales were observed as adherent corrosion product scales. However, detailed examination of composition and morphology of the mixed scales was performed in only one of the three experiments, therefore only the results obtained in this particular experiment were compare against the model prediction in order to verify and verify the model. The experimental test matrix is shown in TABLE 1 below.

In FIGURE 2 measured and predicted corrosion rates are compared for an experiment conducted at T=60°C, pH 6.0, partial pressure of CO_2 p_{CO_2} =7.7 bar, c_{H_2S} =120 ppm in the gaseous phase, $c_{Fe^{2+}}$ = 17 ppm and velocity v=1 m/s. Both the initial corrosion rate and the transient change of corrosion rate can be captured by the model with reasonable accuracy. The initial corrosion was observed to be 0.65 mm/year, which was low due to the retardation by the mackinawite scale formed via solid state reaction. Subsequently the corrosion rate decreased further due to the precipitation of mixed scale, which is shown in FIGURE 3. The scale that formed after 25 days of exposure to system conditions in

multiphase flow was analyzed by EDS. A cross-sectional view of the coupon in FIGURE 3shows three layers of scale and their composition.

When comparing the scale thickness, morphology and composition with the predicted values (FIGURE 4 and FIGURE 5) it is seen that the agreement is good for the thickness of scale (measured: 150 μm, predicted: 160 μm). Moreover, the model also predicts dense mixed scales with three layers of different compositions, with first 10 micron layer consisting of mainly iron carbonate, the second 20 micron layer consists of 70% iron carbonate and 30 % iron sulfide and the third 130 micron layer is made up of mostly iron carbonate. Given the complexity of the process, both the experimental corrosion rate and the scale morphology are matched reasonably well.

The model can also be used to explain the observed multilayer scale. The dominance of iron carbonate in the mixed scale near the metal surface (FIGURE 3) can be explained by investigating the local concentrations of species at different times in the process. Initially the anodic iron dissolution of the corrosion process gradually increases the concentration of Fe^{2+} at the metal surface with respect to time (FIGURE 6), while the cathodic reduction consumes the H^+ and increases pH at the metal surface with respect to time (FIGURE 7). Increased pH leads to the increased concentration of CO_3^{2-} locally (FIGURE 8). Similar is happening with S^{2-} i.e. the concentration also increases with increasing pH. On the other hand, the precipitation processes consume both CO_3^{2-} and S^{2-}. However, CO_3^{2-} is rapidly replenished by the abundant amounts of dissolved CO_2 while S^{2-} is not replenished due to much smaller quantities of dissolved H_2S in the solution so the S^{2-} concentration plummets (FIGURE 9). The replenishment of S^{2-} can be achieved only by transport of S^{2-} from the bulk; however this is slow and is further slowed down as precipitated scales become denser. On balance, the local supersaturation of $FeCO_3$ at the metal surface increases with time (FIGURE 10) due to the increase of both Fe^{2+} and CO_3^{2-} concentration. However, the local supersaturation of FeS decreases and remains close to unity (FIGURE 11), because any excess in S^{2-} is rapidly consumed by the precipitation of FeS. Since the kinetics of both $FeCO_3$ and FeS precipitation depend strongly on the respective supersaturation, $FeCO_3$ will gradually prevail over FeS in the mixed scale when given enough time. This explains the dominance of $FeCO_3$ in the first 60 μm layer next to the metal surface (FIGURE 3). Many similar scenarios of combined CO_2/H_2S corrosion can now be modeled by using the present approach. It should be stressed again that this mode has been calibrated only with a limited number of long term laboratory experiments and further verification and improvement is under way.

EFFECT OF MULTIPHASE FLOW - WATER ENTRAINMENT AND SEPARATION IN OIL-WATER FLOW

Water Entrainment

The simultaneous flow of oil and water in crude oil production and transportation pipelines is a common occurrence, seen anywhere from the well perforations to the final stages of separation. Corrosive gases such as carbon dioxide and hydrogen sulfide are also commonly present in these systems. Typically at low water cuts this is not an issue as all the water is entrained by the flowing oil. As the water cut increases, water “break-out” may occur, leading to segregated flow of separate layers of water and oil phases. Therefore, the possibility of corrosion is high where the water phase wets the pipe wall (typically at the bottom).

In the past, the effect of multiphase oil-water flow on CO_2 corrosion has been considered only in a qualitative sense. Highly turbulent flow at low water cuts was associated with negligible corrosion, whereas low flow rates or intermittent flow at higher water cuts has been associated with corrosion conditions. Hence, it is a challenge for corrosion engineers to determine more precisely the flow conditions leading to corrosion and conversely the conditions leading to entrainment of the free water layer by the flowing oil phase. The other side of this problem: inhibitive effect of certain organic compounds found in crude oils is addressed in a separate paper [4] at the same conference and will not be discussed here.

Little quantitative research has been performed in the past on the subject of water separation and entrainment when considering how significant a factor it is for internal corrosion of mild steel pipelines. Wicks and Fraser (1975)[17] proposed a simplified model for predicting the critical velocity of the flowing oil phase required to sweep out settled water. However, the Wicks and Fraser[17] model is suitable primarily for very low water cut situations. At high water cut, their model underestimates the critical velocity without considering the coalescence of water droplets. Wu[18] (1995) modified Wicks and Fraser[17] model without a big improvement in the performance. Smith et al.[19] (1987) published data that show the ability of some oils to carry water up to 20% water cut, if flowing at velocities larger than 1 m/s. In the CO2 corrosion model of de Waard and Lotz[20] published in 1993, the presence of the hydrocarbon phase was accounted through a so-called water-wetting factor. From the original experiments of Wicks and Fraser[17] a binary prediction factor was extracted suggesting that oil-wetting will occur only for water cuts less than 30% and velocities larger than 1 m/s, when all water can be entrained in the oil phase. In another study published the same year (1993), Adams et al.[21] estimated that below 30% water cut the tubing will be oil-wet; from 30-50%, intermittent water wetting occurs, and over 50% the tubing is water wet. These are very crude criteria that neglect or oversimplify the varying properties of the oil and water phases, the flow regime and the flow geometry. Furthermore, field experience suggests that in some cases corrosion was obtained at water cuts as low as 2%, in others no corrosion was obtained for water cuts as high as 50%. de Waard et al.[22] in 2001 and 2003 updated the original de Waard and Lotz[20] empirical model from 1993 and proposed a new empirical model using an analysis based on the emulsion breakpoint approach. A link between API gravity, emulsion stability and water wetting of steel by an oil-water mixture was considered by taking into account the changes in interfacial tensions in an oil-water-steel system. This was a major step forward from the original model, however, while agreeing reasonably well with the specific pool of field cases used for its calibration, the new model remains an empirical correlation built on limited field data with an uncertain potential for extrapolation. More importantly, this model does not consider the effect of pipe diameter, oil density, oil viscosity and system temperature on the critical velocity of the flowing oil phase required for entrainment. It can be argued though that the simplified Wicks and Fraser[17] model gave critical velocities which did not depend much on diameter and viscosity and that density and viscosity are inversely correlated.

To understand the mechanism of water entrainment in the oil-water pipe flows, it is necessary to look closer into different flow regimes that occur. The main difficulties in understanding and modeling of the behavior of oil-water flows arise from the existence of the interfaces between the phases. The internal structures of two-phase flow can be best described by the flow patterns. The momentum and mass transfer mechanisms between the two phases significantly depends on the flow patterns. Also, flow patterns can indicate the phase wetting the pipe wall, position of the phases and the degree of mixing during the flow. Compared to gas-liquid flow studies, a fewer studies[23-40] are dedicated to flow of two immiscible liquids such as water and oil. Nevertheless, there is enough understanding of the flow

dynamics to give us an opportunity to formulate a model that goes beyond the initial effort of Wicks and Fraser[17].

Various flow patterns observed in the horizontal pipe flows are given in the FIGURE 12. Stratified flow with a complete separation of water and oil phases may exist at very low flow rates where the stabilizing gravity force due to a finite density difference is dominant. With increasing the flow rate, the interface displays a wavy character with possible entrainment of droplets at one side or both sides of the interface (semi-stratified flow). The entrainment processes for both phases increase with the flow rates. When the pure water and oil layers are still continuous at the bottom and top of the pipe respectively, and a layer of dispersed droplets exists at the interface, a three-layer structure is formed. At sufficiently high oil flow rate and low water cut, the entire water phase becomes discontinuous in a continuous oil phase resulting in a water-in-oil dispersion. Vice versa, at sufficiently high water flow rate and a high water cut, the entire oil phase becomes discontinuous in a continuous water phase resulting in an oil-in-water dispersion. There are operating conditions under which an oil-in-water dispersion will change to water-in-oil dispersion. This phenomenon is referred by lots of researchers as “phase inversion” and is associated with an abrupt change in the frictional pressure drop and a switch of the phase wetting the pipe wall from water to oil phase.

In upward and downward vertical flows, the distribution of oil water phases has a nearly cylindrical symmetry. The observed flow patterns (shown in the FIGURE 13) typically include unstable water-in-oil (oil dominated) and oil-in-water (water dominated) dispersed flow at low oil-water mixture velocity and stable oil-in-water and water-in oil dispersed flows at high oil-water mixture velocity. In the unstable dispersed flows, the water drops and oil drops occasionally contact the pipe wall because of the effect of flow turbulence. In the unstable oil-in-water dispersed flow, water phase always wets the pipe wall. Similarly, oil wets the pipe wall when unstable water-in-oil dispersed flow occurs. On the other side, in both types of unstable dispersed flows, the size of the dispersed drops is relatively large because of low turbulence and shear force, large water or oil slugs may exist. Increasing the oil-water mixture velocity leads to smaller dispersed drops, and eventually at high oil-water mixture velocity either stable homogeneous water-in-oil dispersion (if oil is the continuous phase) or stable oil-in-water dispersion (if water is the continuous phase) is formed.

In the upward inclined oil-water pipe flows, the flow structure is more complicated than those in the horizontal and vertical flows. The key parameter influencing the structure of such deviated flows is the presence of gravity-driven buoyancy effects. In some cases, the lighter phase (generally oil phase) gathers ate the upper portion of pipe cross-section. Heavier phase (water phase) tends to flow at the bottom of pipe. In addition, the fluid velocity is non-uniform across the pipe. The existence of gravitational component at an angle to the flow direction, in addition to pressure and viscous forces, leads to numerous flow patterns with unique hydrodynamic characteristics. For instance, at low oil and water velocities, the presence of countercurrent water flow (J. Flores[33] and Vigneaux etal.[35]) at the bottom side of pipe exists. Since oil-water stratified flow does not exist in the upward inclined pipe flows, two main flow patterns will be considered in the present study: unstable and stable oil-water dispersed flows (shown in FIGURE 14).

The flow patterns in the downward inclined oil-water flows are similar with those in the horizontal pipe flows. At low water-oil mixture velocity and small pipe inclination, stratified flow exists. With increasing the flow rate, the interface displays a wavy character with possible entrainment of droplets at one side or both sides of the interface (semi-stratified flow). The entrainment processes for both phases increase with the flow rates. When the pure water and oil layers are still continuous at the bottom and top of the pipe respectively, and a layer of dispersed droplets exists at the interface, a three-

layer structure is formed. At sufficiently high oil flow rate and low water cut, the entire water phase becomes discontinuous in a continuous oil phase resulting in a water-in-oil dispersion. Vice versa, at sufficiently high water flow rate and a high water cut, the entire oil phase becomes discontinuous in a continuous water phase resulting in an oil-in-water dispersion. On the other side, even at low oil-water mixture velocity, stratified flow gradually disappears with increasing the pipe inclination since oil and water phases mix much easier and tend to form dispersed flow because of the effect of gravity force. The phase with lower flow rate will be dispersed into the phase, which flows with higher flow rate. The phase with higher flow rate wets the pipe wall.

To account for this complexity and to extract a valid criterion for water separation and entrainment a new approach following Brauner[41] and Barnea[43] has been adopted. A criterion for forming stable water-in-oil dispersed flow is derived as the means of calculating the critical velocity for water entrainment. Two main physical properties, maximum droplet size, d_{max}, related to breakup and coalescence and critical droplet size, d_{crit}, related to settling and separation are compared to deduce this criterion. Since water is entrained by the flowing oil phase in the form of droplets, it is essential to know the maximum droplet size d_{max} that can be sustained by the flow without further breakup. In dilute water-in-oil dispersion d_{max} evolves from a balance between the turbulent kinetic energy and the droplet surface energy. For the dilute dispersion Brauner[41] shows that:

$$\left(\frac{d_{\max}}{D}\right)_{dilute} = 1.88\left[\frac{\rho_o(1-\varepsilon_w)}{\rho_m}\right]^{-0.4} We_o^{-0.6}\,\mathrm{Re}_o^{0.08} \tag{18}$$

Where:

$$\mathrm{Re}_o = \frac{\rho_o D U_c^2}{\eta_o} \qquad We_o = \frac{\rho_o D U_c^2}{\sigma}$$

where D and d_{max} denote the pipe diameter and maximum droplet size, respectively, in m. ε_w presents the water cut. ρ denotes the density of liquid, in $kg\ m^{-3}$. The subscripts o, m and *dilute* present the oil phase, the oil-water mixture and dilute oil-water dispersion, respectively. f is the friction factor. η_o denotes the viscosity of oil phase, in $Pa.s$. σ presents the oil surface tension, in Nm^{-1}.

It is noted that this equation can be only used in the dilute dispersions i.e. as long as it satisfies the following condition:

$$(1-\varepsilon_w)\frac{\rho_o}{\rho_m} \cong 1 \tag{19}$$

In dense dispersions, droplet coalescence takes place. Under such conditions, the flowing oil phase disrupts the tendency of the water droplets to coalesce. Brauner[41] has shown that this leads to:

$$\left(\frac{d_{\max}}{D}\right)_{dense} = 2.22 C_H^{0.6}\left(\frac{\rho_o U_c^2 D}{\sigma}\right)^{-0.6}\left(\frac{\varepsilon_w}{1-\varepsilon_w}\right)^{0.6}\left[\frac{\rho_m}{\rho_o(1-\varepsilon_w)} f\right]^{-0.4} \tag{20}$$

where U_c denotes the velocity of continuous phase, in ms^{-1}. C_H is a constant with the order of one, $O(1)$. D and d_{max} denote the pipe diameter and the maximum droplet size, respectively, in m. ε_w presents the water cut. ρ denotes the density of liquid, in $kg\ m^{-3}$. The subscripts o, m and *dilute* present the oil phase, the oil-water mixture and dilute oil-water dispersion, respectively. σ presents the oil surface tension, in Nm^{-1}. f is the friction factor:

$$f = 0.046/\mathrm{Re}_o^{0.2} \tag{21}$$

Thus, given a water-oil fluid system and operational conditions, the maximum droplet size that can be sustained is the larger of the two values obtained via (18) and (20), which can be considered as the worst case for a given oil-water system:

$$\frac{d_{\max}}{D} = Max\left\{\left(\frac{d_{\max}}{D}\right)_{dilute}, \left(\frac{d_{\max}}{D}\right)_{dense}\right\} \tag{22}$$

Droplets larger than a critical droplet size d_{crit} separate out from the two-phase flow dispersion either due to gravity forces, predominant in horizontal flow, or due to deformation and "creaming" typical for vertical flow[43]. *Critical droplet diameter*, d_{cb}, above which separation of droplets due to gravity takes place can be found via a balance of gravity and turbulent forces as[43]:

$$\left(\frac{d_{cb}}{D}\right) = \frac{3}{8}\frac{\rho_o}{|\Delta\rho|}\frac{fU_c^2}{Dg\cos(\theta)} = \frac{3}{8}f\frac{\rho_o}{\Delta\rho}Fr_o \tag{23}$$

Where Froude number is:

$$Fr_o = \frac{U_c^2}{Dg\cos(\theta)}$$

and

$$\Delta\rho = |\rho_o - \rho_w|$$

Where D and d_{cb} denote the pipe diameter and the *critical droplet size*, respectively, in m. ρ denotes the density of liquid, in $kg\ m^{-3}$. The subscripts *o and w* present the oil phase and water phase, respectively and θ denotes the inclination of pipe, in *degree*.

This effect is predominant at low pipe inclinations i.e. in horizontal and near-horizontal flows. Critical droplet diameter, $d_{c\sigma}$, above which drops are deformed and "creamed", leading to migration of the droplets towards the pipe walls in vertical and near-vertical flows, can be calculated with the equation proposed by Brodkey[44]:

$$\left(\frac{d_{c\sigma}}{D}\right) = \left[\frac{0.4\sigma}{|\rho_o - \rho_w| gD^2\cos(\beta)}\right]^{0.5} \tag{24}$$

$$\beta = \begin{cases} |\theta| & |\theta| < 45^o \\ 90 - |\theta| & |\theta| > 45^o \end{cases}$$

Where D and $d_{c\sigma}$ denote the pipe diameter and the *critical droplet size*, respectively, in *m*. ρ denotes the density of liquid, in *kg* m^{-3}. The subscripts *o and w* present the oil phase and water phase, respectively. *f* is the friction factor. θ denotes the inclination of pipe, in *degree*. σ presents the oil surface tension, in Nm^{-1}.

The critical droplet diameter, d_{crit}, can then be conservatively estimated for any pipe inclination according to the suggestion made by Barnea[43] (1987):

$$\frac{d_{crit}}{D} = Min \left\{ \left(\frac{d_{cb}}{D} \right), \left(\frac{d_{c\sigma}}{D} \right) \right\} \tag{25}$$

At this point the final criterion for entrainment emerges. The transition from stratified flow to stable water-in-oil dispersion takes places when the oil phase turbulence is intense enough to maintain the water phase broken up into droplets not larger then d_{max} which has to be smaller than the a critical droplet size d_{crit} causing droplet separation. The transition criterion is then (Brauner[41], 2001):

$$d_{\max} \le d_{crit} \tag{26}$$

Equations (22) and (25) into (26) give means to determine the critical velocity.

Water Separation

If the water phase is not entirely entrained and flows separated from oil phase, for corrosion calculations it is crucial to predict the water scale velocity, water film thickness and the area of the internal pipe wall wetted by water at different flow regimes.

Stratified oil-water mixture structure exists in the horizontal and downward inclined pipe flows (FIGURE 12 and FIGURE 14). Neogi et al.[45] and Taitel et al.[46] proposed a three-layer segregated flow model to calculate the thickness of water layer for gas-water-oil three-phase stratified flow. They considered water, oil and a mixed layer in between as three different "phases" with each phase having its own distinct properties. Also, they proposed that the interfaces between the pure water layer / oil-water mixed layer / pure oil layer are all flat. D. Vedapuri et al.[47] used this three-layer segregated flow model to calculate the thickness of water layer and in-situ water cut for oil-water flows. Shi et al.[48] proposed a four-layer segregated flow model for calculating in-situ water, water film thickness and water film in-situ velocity by further dividing the mixed layer into two different layers: water-in-oil and oil-in-water dispersions. They assumed that these two layers are homogeneous and also treated all the interfaces as flat. It should be pointed out that while appealing, Shi et al.[48] four-layer approach gives rise to further difficulties when trying to calculate interfacial shear stresses. Also, from the viewpoint of the corrosion process, water droplets suspended in this mixed layer do not contribute to corrosion and can be ignored. Therefore, in this study, the model is based on a three-layer flow structure (FIGURE 15). All the interfaces are considered to be flat as proposed by Neogi et al.[45] and Taitel et al.[46]. The details of the theory are given elsewhere[52]. In a nutshell, the momentum and mass balances for oil, water and oil-water mixed layer are solved simultaneously to obtain the in-situ velocities for pure water layer, oil-water

mixed layer and pure oil layer, as well as the thickness of pure water layer and the corresponding water wetted pipe cross-section area. All these information are very crucial to the corrosion prediction.

Phase Inversion

At very high water cuts (typically larger than 40-50%) oil-in-water flow structure can be found at all pipe inclinations Water is the continuous phase and the oil phase is dispersed and entrained by the flowing water phase. The criterion used to calculate the water cut when inversion occurs is[28]:

$$\varepsilon_{invert} = 0.5 - 0.1108 \log_{10}(10^3 \eta_o) \quad (27)$$

Where ε_{invert} denotes the water cut at phase inversion point. η_o denotes the viscosity of oil phase, in *Pa.s*.

Validation

Comparison with Laboratory Data

A comparison between the experimental results and predictions made by the water entrainment model for different flow regimes was done. All the experimental results were obtained from Trallero et al.[32], Flores[34], Nadler and Mewes[36], Angeli and Hewitt[37], Shi et al.[48] and a large in-house database of oil-water flows[53]. TABLE 2 summarizes the important parameters in these experiments.

In the horizontal pipe flows, the model predicts the experimentally observed stratified flow pattern[32, 36, 37, 48] with an accuracy of 80% (40 out of 50 cases). For water-in-oil dispersed flow a somewhat weaker agreement between the predictions and experimental data is seen with an agreement of 70% (35 out of the 50 cases simulated).

In the upward vertical pipe flow, the model predicts the experimentally observed water-in-oil dispersed and oil-in-water dispersed flow patterns with an accuracy of 90% (108 out of 120 cases[34]). Similarly, in the upward inclined pipe flows, the model predicts the experimentally observed water-in-oil and oil-in-water dispersed flow patterns with an accuracy of 80% (96 out of 120 cases[34]). It should be clearly pointed out that very fine dispersion water-in-oil and oil-in-water flow patterns defined by Flores[34] are equivalent to stable water-in-oil and oil-in-water dispersed flows in this study respectively. The other flow patterns defined by Flores[34] in the vertical pipe flow are all treated as unstable water-in-oil and oil-in-water dispersed flows. From the corrosion point of view, all these simplifications are reasonable based on the phase wetting mechanism for corrosion prediction.

Comparisons were made between the predicted results by the three-layer model described above and experimental data for the pure water layer thickness (taken from the water/oil flow measurements[53]) at input water cuts ranged from 0% and 80%. All the experimental parameters were described in the reference[53] in TABLE 2. The oil-water mixture velocity flow rate was in the range of 0.45 - 1.8 m/s. The comparisons between experimental results[53] and the predictions for the water film height in horizontal flows are depicted in the FIGURE 16 and FIGURE 17. It can be concluded that the model slightly underestimates the water film heights with different discrepancies at different water cuts and velocities. Very good agreement between the experimental results and the predictions are achieved at higher water cut and lower velocity. Higher discrepancy occurs at lower water cut and higher mixture velocity. Reasonable agreements (FIGURE 18 to FIGURE 19) have been achieved between experimental results

and the predictions in downward inclined pipe flows. Higher accuracy of prediction occurs at higher water cuts than that obtained at lower water cuts.

Comparison with Field Data

A comparison between field data and predictions made by the current model for the critical velocity of water entrainment by flowing oil phase was done. All field data were obtained from Gunaltun[51]. TABLE 3 summarizes the important parameters, such as flow conditions, along with water compositions. Based on the flow conditions from the wells, Gunaltun[51] used the Wicks and Fraser[17] model to estimate the critical velocity for water entrainment by the oil in the tubing. He found out that the critical velocities in bottomhole and wellhead conditions were respectively 0.4 m/s and 0.5 m/s. With same parameters in the TABLE 3 the critical velocity calculated with present model is much higher than that with the Wicks and Fraser[17] model. The critical velocity varies from 0.9 to 1.6 m/s, depending on the well deviation and water cut. Based on the corrosion field data[51,] the Wicks and Fraser[17] model significantly underestimates the critical velocity for water entrainment since corrosion was found at the velocity of 0.5 m/s or even higher. Obviously, the current multiphase flow model offers a more reliable prediction of water separation for the pool of field cases reported by Gunaltun[51].

According to the corrosion rate predictions done with the present model, the corrosion rate ranges from 0.54 to 4.56 mm/y (shown in the shaded area in FIGURE 20). Some of the required data from the field were known only approximately so ranges of input parameters were used to cover the domain of interest. Compared to corrosion field data (FIGURE 20, Y. Gunaltun[51]), it is clear that most of the values are smaller than 4 mm/y except for a few points that were located within the range between 4 and 7 mm/y. It can be concluded that the predictions with the present model are in reasonable agreement with the reported field data given all the uncertainties involved in the comparisons.

Parametric Testing

Parametric testing of the two-phase oil-water flow model was done to highlight the effect of some key parameters on water entrainment as well as the effect on corrosion rate. FIGURE 21 shows the effect of water cut on critical water entrainment velocity for a hypothetical light crude oil with API around 41. Increasing water cut leads to a higher critical velocity of flowing oil phase required for water entrainment. The commonly mentioned 1 m/s threshold is recovered in this case only for very low water cuts. It should be noted that the curve shown in FIGURE 21 is valid only for the particular combination of parameters listed there and the actual numbers change when any of the parameters is modified, however, without changing the character of the overall dependence. This holds of all of the simulations discussed below.

The effect of oil density on the critical velocity is shown in FIGURE 22. Increasing oil density significantly decreases the critical velocity. As the oil density approaches that of water, the miscibility between oil and water increases. The momentum and mass exchange between them is much easier, i.e. water can be much easier entrained and suspended by a heavy oil phase. FIGURE 23 shows effect of Oil API (oil density) on the maximum water cut carried by the flowing oil phase. Increasing the oil API leads to a significant decrease of the maximum amount of water entrained by the flowing oil phase. The maximum water cut ranges from 2% to approximate 30% with respect to different oil APIs.

FIGURE 24 shows the effects of oil surface tension on the critical velocity. Decreasing oil surface tension by adding surfactants (such as corrosion inhibitors) will decrease the critical velocity. Low surface tension corresponds to low surface energy of droplets. This means that lower turbulent

kinetic energy, which is proportional to low flow rate of the flowing oil phase, is needed to deform and breakup the droplets and keep them suspended. FIGURE 25 shows the effect of oil-water surface tension on the maximum water cut carried by the flowing oil phase. The maximum water cut for water entrainment increase from 0.5% to 14.1% when the oil-water surface tension decreases from 0.1 to 0.001 N/m what can happen for example by adding a corrosion inhibitor.

When all the water is entrained by the flowing oil the scale of the corrosion problem is much smaller or can be ignored. However, let us see how the corrosion rate is affected below the critical velocity when there water flows segregated from the oil phase. FIGURE 26 shows the relation between corrosion rate and oil flow rate at pH= 4 in oil-water horizontal flow. Increasing superficial oil velocity from 0.1 to 1.25 m/s leads to an increase of corrosion rate from 1.67 to 5.58 mm/yr. This is because at the selected pH4 the corrosion rate is very sensitive to mass transfer and turbulent mixing which are in turn enhanced at higher flow rates (at higher pH the flow dependency of the corrosion rate decreases). Calculated trend of in-situ water film velocity shown in FIGURE 27 indicates that as the oil flow velocity is increased the water layer also accelerates (with a lag). Corrosion rate dramatically decreases with increasing oil velocity beyond 1.2 m/s and eventually no corrosion occurs at 1.4 m/s when the water is totally entrained by the flowing oil phase. The trend of in-situ water film thickness shown in FIGURE 27 indicates that increasing oil velocity leads to a decrease of water film thickness and above 1.2 m/s this effect “overpowers” the increasing velocity leading to a decrease in turbulent mixing and a drop in the corrosion rate. Again it must be stressed that the numbers shown here are valid only for the particular combination of parameters used in this case and would change when any of the key parameters is modified.

CONCLUSIONS

- A comprehensive integrated CO_2 / H_2S corrosion – multiphase flow model package has been presented that takes into account the effect of most important variables and processes.
- The model can account for formation of iron carbonate and iron sulfide scales and predict their morphology as well as the effect on the corrosion rate.
- A model can successfully predict the critical velocity for entraining free water by the flowing oil phase as well as the effect of the key variables.
- The model has been extensively calibrated with laboratory data and compared with limited field data.

ACKNOWLEDGEMENT

The authors would like to acknowledge the contribution of the consortium of companies whose continuous financial support and technical guidance led to the publishing of this work. They are BP, ConocoPhillips, ENI, Petrobras, Saudi Aramco, Shell, Total, Champion Technologies, Clariant, MI Technologies and Nalco.

REFERENCES

1 C. de Waard and D.E. Milliams, Corrosion, 31 (1975): p131.

2. R. Nyborg: “Overview of CO_2 Corrosion Models for Wells and Pipelines”, CORROSION/2002, paper no. 233 (Houston, TX: NACE International, 2002).

3 S. Nesic, S. Wang, J. Cai and Y.Xiao, “Integrated CO_2 Corrosion – Multiphase Flow Model”, NACE 2004, Paper No.04626, pp. 1-25, 2004.

4 Hernandez, S., Nesic, S., Weckman, G. and Ghai, V., “Use of Artificial Neural Networks for Predicting Crude Oil Effect on CO2 Corrosion of Carbon Steels”, NACE 2005, Paper No.05554, 2005.

5 Y. Xiao and S. Nesic, “A Stochastic Prediction Model of Localized CO_2 Corrosion”, NACE 2005, Paper No.05057, 2005.

6 J. Lee and S. Nesic “The Effect of Trace Amounts of H2S on CO2 Corrosion Investigated by Using the EIS Technique”, NACE 2005, Paper No.05630, 2005.

7. M. Nordsveen, S. Nesic, R. Nyborg and A. Stangeland, “A Mechanistic Model for Carbon Dioxide Corrosion of Mild Steel in the Presence of Protective Iron Carbonate Films - Part1: Theory and Verification”, Corrosion, Vol. 59, (2003): p. 443.

8. S. Nesic, M. Nordsveen, R. Nyborg and A. Stangeland, "A Mechanistic Model for CO_2 Corrosion of Mild Steel in the Presence of Protective Iron Carbonate Films - Part II: A Numerical Experiment", Corrosion, Vol. 59, (2003): p. 489.

9. S. Nesic, K.-L.J.Lee, "A Mechanistic Model for CO2 Corrosion of Mild Steel in the Presence of Protective Iron Carbonate Films - Part Ⅲ: Film Growth Model", Corrosion, Vol. 59, (2003): p. 616.

10. J. T. Davies, Turbulence Phenomena, (Academic Press, 1972).

11. S. Nesic, J. Postlethwaite, S. Olsen, Corrosion, “An Electrochemical Model for Prediction of Corrosion of Mild Steel in Aqueous Carbon Dioxide Solutions”, 52, (1996): p. 280.

12. S. Nesic, N. Thevenot, J.-L. Crolet, D. Drazic, "Electrochemical Properties of Iron Dissolution in the Presence of CO_2 - Basics Revisited", CORROSION/96, paper no. 3, (Houston, TX: NACE International, 1996).

13. D.W. Shoesmith, P. Taylor, M.G. Bailey, D.G. Owen, J. Electrochem. Soc. 127 (1980) p.1007.

14. E.W.J. van Hunnik, B.F.M. Pots and E.L.J.A. Hendriksen, "The Formation of Protective FeCO3 Corrosion Product Layers in CO2 Corrosion". CORROSION/96, paper no. 6, (Houston, TX: NACE International, 1996).

15. N.G. Harmandas and P.G. Koutsoukos, “The formation of iron sulfides in aqueous solutions”, Journal of Crystal Growth, 1996, p.719.

16. B. Brown, “CO_2/H_2S corrosion in supersaturated conditions” Oct. 2004, Institute of Corrosion and Multiphase Technology Board Meeting report, Ohio University.

17 Wicks, M., and Fraser, J.P., “Entrainment of Water by Flowing Oil”, Materials Performance, May 1975, pp. 9~12.

18 Wu, Y., “Entrainment Method Enhanced to Account fro Oil’s Water Content”, Oil & Gas Technology, Aug. 28, 1995, pp. 83~86.

19 L.M.Smith, M.J.J. Simon Thomas and C. de Waard, “Controlling Factors in the Rate of CO2 Corrosion”, UK. Corr.’87 Brighton, 26-28 Oct., 1987

20 C. de Waard and U. Lotz, “Prediction of CO2 Corrosion of Carbon Steel”, Corrosion/93, paper no. 69, (Houston, TX: NACE International, 1993)

21 C. D. Adams, J. D. Garber, F. H. Walters, C. Singh, “Verification of Computer Modeled Tubing Life Predictions by Field Data”, Corrosion/93, paper no. 82, (Houston, TX: NACE International, 1993)

22 C. de Waard, L. Smith and B.D. Craig, “The Influent of Crude Oil on Well Tubing Corrosion Rates”, EUROCORR 2001

23 Russell, T. W. F., Hodgson, G.W., and Govier, G. W., “Horizontal Pipelines Flow of Mixtures of Oil and Water”, Can. J. of ChE, 37, 9-17, 1959

24 Charles, M.E., Govier, G.W. and Hodgson, G.W., “The Horizontal Pipelines Flow of Equal Density Oil-water Mixture”, Can. J. Chem. Eng., 39, 27-36, 1961

25 Ward, J.P. and Knudsen, J.G, “Turbulent Flow of Unstable Liquid-Liquid Dispersions: Drop Size and Velocity Distributions”, AIChE. J., 13, No 2, 356-367, 1967

26 Oglesby, K. D., “An Experimental Study on the Effects of Oil Viscosity, Mixture Velocity and Water Fraction on Horizontal Oil-Water flow”, M.S. Thesis, University of Tulsa, 1979

27 Mukherjee, H., Brill, J.P., and Beggs, H. D., “Experimental Study of Oil-Water Flow in Inclined Pipes”, J. of Energy Resources Technology, 56-66, March, 1981

28 Arirachakaran, S., K. D., Oglesby, M. S., Malinovsky, M.S., Shoham, O., and J.P. Brill, “An Analysis of Oil-Water Flow Phenomena in Horizontal Pipes”, SPE paper 18836, 155-167, 1989

29 Pal, R., “Pipeline Flow of Unstable and Surfactant-Stabilized Emulsions”, AIChE J., 39, No.11, 1754-1764, 1993

30 Pal, R., “Effect of Droplet Size on the Rheology of Emulsions”, AIChE J., 42, No.11, 3181-3190, 1996

31 Kurban, A. P. A., Angeli, P. A., Mendes-tatsis, M. A., and Hewitt, G. F., “Stratified and Dispersed Oil-Water Flows in Horizontal Pipes”, Multiphase 95, 277-291, 1995

32 Trallero, J. L, Sarica, C and J. P. Brill, “A Study of Oil-Water Flow Patterns in Horizontal Pipes”, SPE, Paper No. 36609, 363-375, 1996

33 Flores, J. G., Sarica, C., Chen, T. X., and Brill, J. P., “Investigation of Holdup and Pressure Drop Behavior for Oil-Water Flow in Vertical and Deviated Wells”, ETCE-98, Paper No. 10797, 1997

34 Flores, J. G., “Oil-Water Flow in Vertical and Deviated Wells”, Ph.D Thesis, University of Tulsa, 1997

35 Vigneaux, P., Chenais and Hulin, J.P., “Liquid-liquid Flows in an Inclined Pipe”, AICHE Journal, Vol.34, No.5, 781-789, 1988

36 Nadler, M. and Mewes, D, “Flow Induced Emulsification in the Flow of Two Immiscible Liquids in Horizontal Pipes”, Int. J. Multiphase Flow, 23, 56-68, 1997

37 Angeli, P., and Hewitt, G. F, “Drop Size Distributions in Horizontal Oil-Water Dispersed Flows”, Chem. Eng. Sci. 55, 3133-3143, 2000

38 Corlett, A.E., and Hall, A.R.W., “Viscosity of Oil and Water Mixtures”, Multiphase 99, 595-603, 1999

39 H.Shi, “A Study of Oil-Water Flows in Large Diameter Horizontal Pipelines”, Ph.D Dissertation, Ohio University, 2001

40 Brauner, N., Moalem Maron, “Flow Pattern Transitions in Two-phase Liquid-liquid Horizontal Tubes”, Int. J. of Multiphase Flow, Vol.18, pp. 123~140(1992a).

41 Brauner, N., “The Prediction of Dispersed Flows Boundaries in Liquid-Liquid and Gas-liquid Systems”, Int. J. of Multiphase Flow, Vol.27, pp. 885~910(2001)

42 Hinze, J., “Fundamentals of the Hydrodynamic Mechanism of Splitting in Dispersion Process”, AICHE, Vol. 1(1955), No. 3, pp. 289~295

43 Barnea, D., “A Unified Model for Predicting Flow Pattern Transitions for the Whole Range of Pipe Inclinations”, Int. J. of Multiphase Flow, Vol.11, pp. 1~12(1987)

44 Brodkey, R.S., “The Phenomena of Fluid Motions”, Addison-Wesley, Reading, M.A., 1969

45 Neogi, S., Lee, A.H. and Jepson, W.P., “A Model for Multiphase (Gas-Water-Oil) Stratified Flow in Horizontal Pipelines”, SPE 28799, pp.553-561, 1994

46 Taitel, Y., Barnea, D. and Brill, J.P., “Stratified Three-phase Flow in Pipes”, Int. J. Multiphase Flow, Vol. 21, No.1, pp. 53-60, 1995

47 D. Vedapuri, D. Bessette and W.P. Jepson, “A Segregated Flow Model to Predict Water Layer Thickness in Oil-Water Flows in Horizontal and Slightly Inclined Pipelines”, Multiphase’97, pp. 75-105.

48 Hua Shi, Hongbin Wang and W.P. Jepson, “Prediction of water Film Thickness and Velocity for Corrosion Rate Calculation in Oil-Water Flows”, NACE 2002, Paper No.02500, pp. 1-18, 2002

49 Taitel, Y. and Dukler, A.E., “A Model for Predicting Flow Regime Transitions in Horizontal and Near Horizontal Gas Liquid Flow”, AICHE J., Vol.22, No.1, pp.47, 1976

50 N. Brauner and Maron, D.M., “Two-phase Liquid-liquid Stratified Flow”, Physicochemical Hydrodynamics, Vol. 11, No.4, pp.487-506, 1989.

51 Y. Gunaltun, “Carbon Dioxide Corrosion in Oil Wells”, SPE 21330, pp.97-113, 1991.

52 Jiyong Cai, Srdjan Nesic and Cornelis de Waard, “Modeling of Water Wetting in Oil-Water Pipe Flow”, NACE 2004, Paper No.04663, pp. 1-19, 2004.

53 Flow Database in Oil-water flows, Private Report, Institute for Corrosion and Multiphase Technology, Ohio University, 2004.

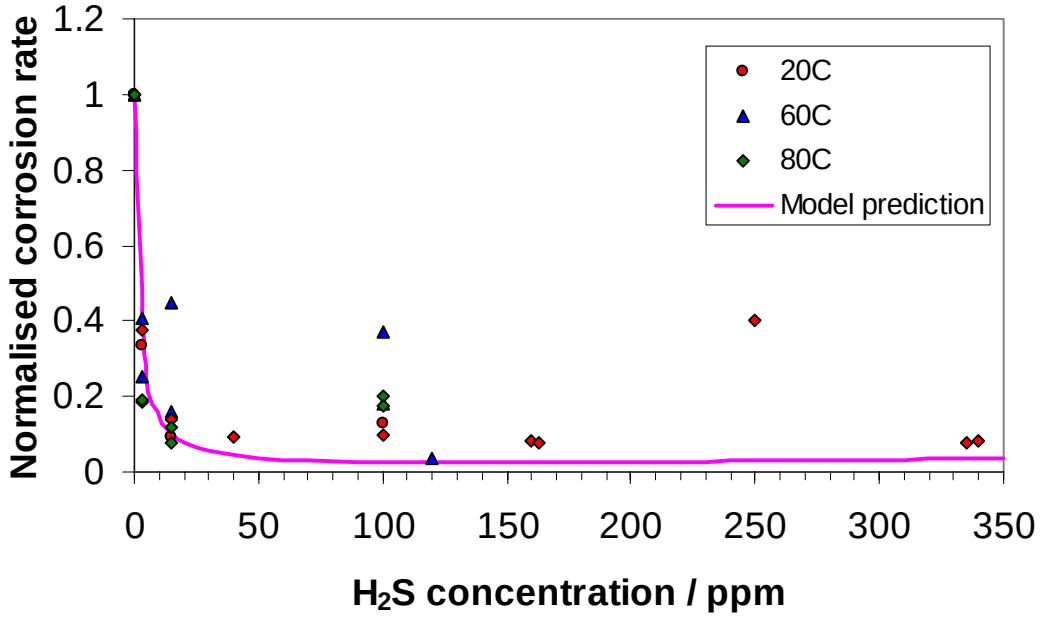

FIGURE 1. Comparison between model prediction and experimental data on the effect of trace amount of H_2S on CO_2 corrosion rate in the absence of iron sulfide scales: pH<5, P_{CO_2} = 1-7.7 bar, T = 20-80°C, v=stagnant to 3 m/s. ppm refers to the concentration in the gas phase.

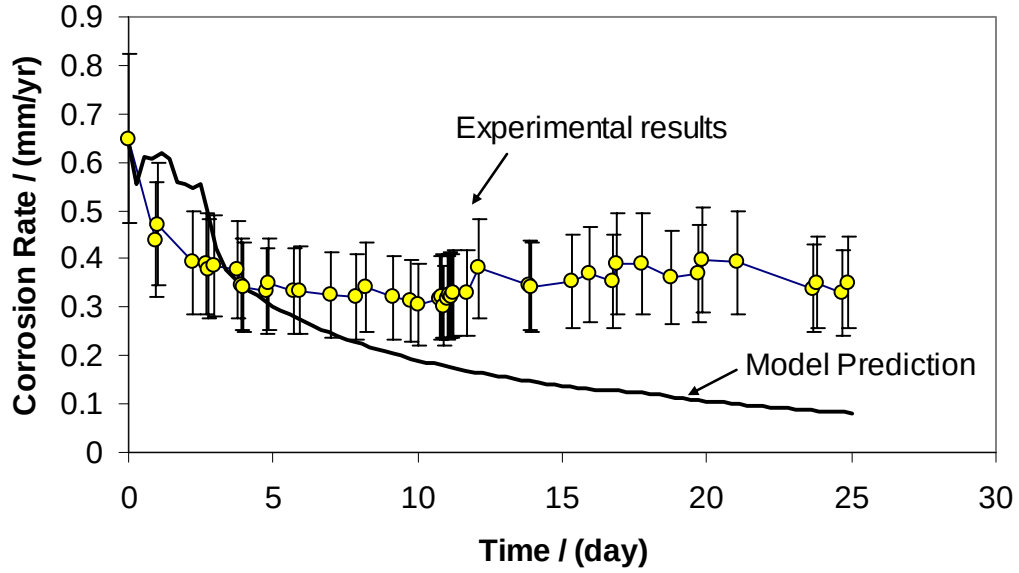

FIGURE 2. Comparison between the model prediction and the measured corrosion rate in the presence of trace amount of H_2S at scale forming initial conditions: pH 6 in saturated CO_2 solution with 120 ppm gaseous H_2S, water + 1% NaCl, P_{CO_2} = 7.7 bar, T = 60°C, Fe^{2+}=17ppm.

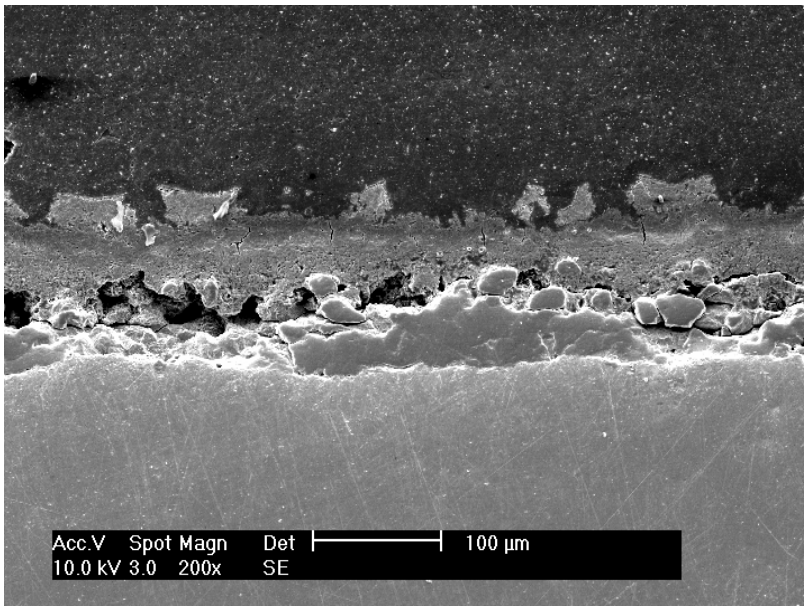

FIGURE 3. Examination of cross section composition of X65 coupon after 25 day of exposure using EDS, at initial conditions of pH 6 in saturated CO_2 solution with 120 ppm gaseous H_2S, water + 1% NaCl, P_{CO_2} = 7.7 bar, T = 60°C, Fe^{2+}=17ppm. Composition of layer #1 (next to metal surface): 60 um, layer #2: 60 um, and layer #3: 30 um. Layer #1 is [32.4% Fe, 0.0% S, 13.4% C, 26.5% O], the interface between layer #1 and layer #2 is [35.4% Fe, 12.9% S, 14.0% C, 9.5% O], and of layer #2 is [31.2% Fe, 15.0% S, 20.8% C, 11.2% O].

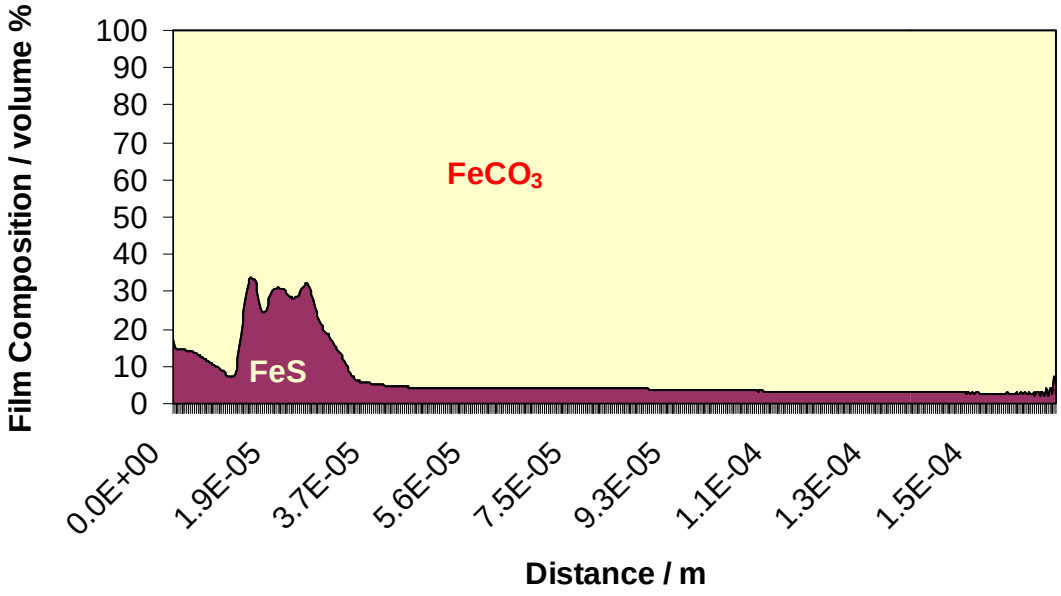

FIGURE 4. Predicted scale (film) thickness and composition of scale after 25 days of exposure at initial conditions of c_{H_2S} =120 ppm, T=60°C, P_{CO_2} = 7.7bar, pH 6.0, $c_{Fe^{2+}}$ =17 ppm, v=1 m/s.

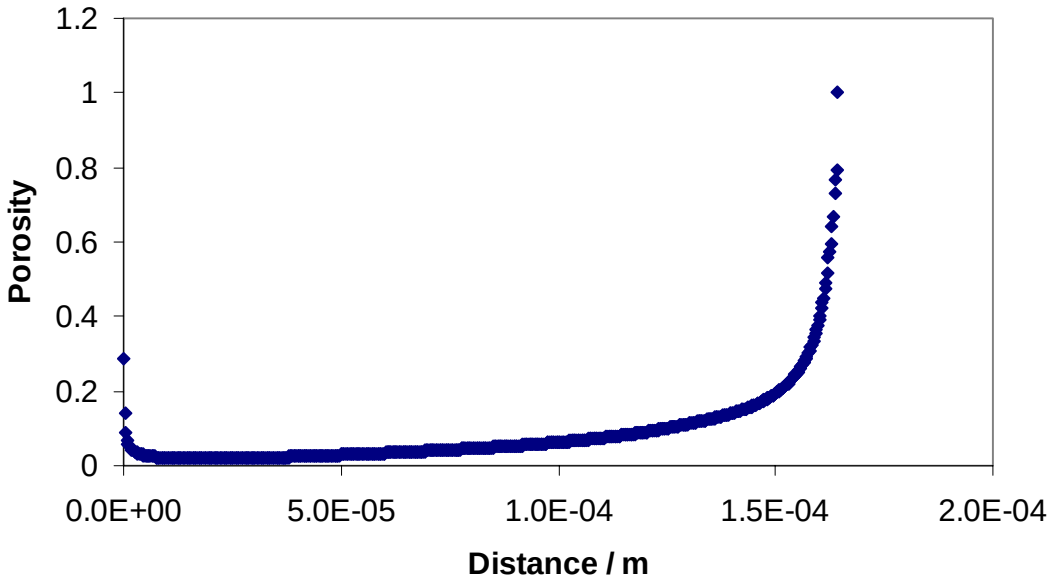

FIGURE 5. Predicted scale thickness and porosity of scale after 25 days of exposure at initial conditions of c_{H_2S} =120 ppm, T=60°C, P_{CO_2} = 7.7bar, pH 6.0, $c_{Fe^{2+}}$ =17 ppm, v=1 m/s. Porosity ε=1 means no scale.

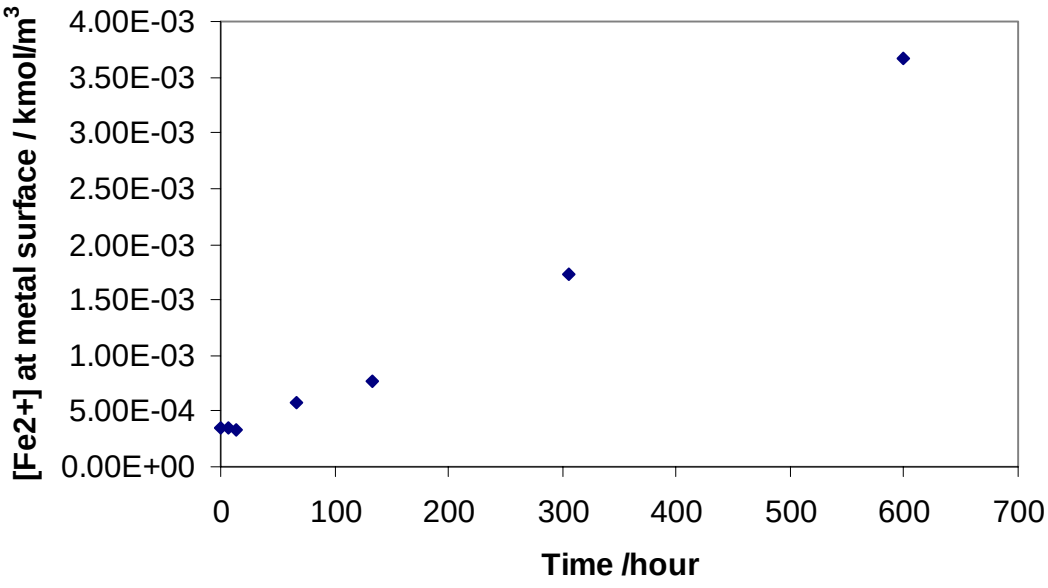

FIGURE 6. Predicted change of concentration of Fe^{2+} at the metal surface with respect to time at initial conditions of c_{H_2S} =120 ppm, T=60°C, P_{CO_2} = 7.7bar, pH 6.0, $c_{Fe^{2+}}$ =17 ppm, v=1 m/s.

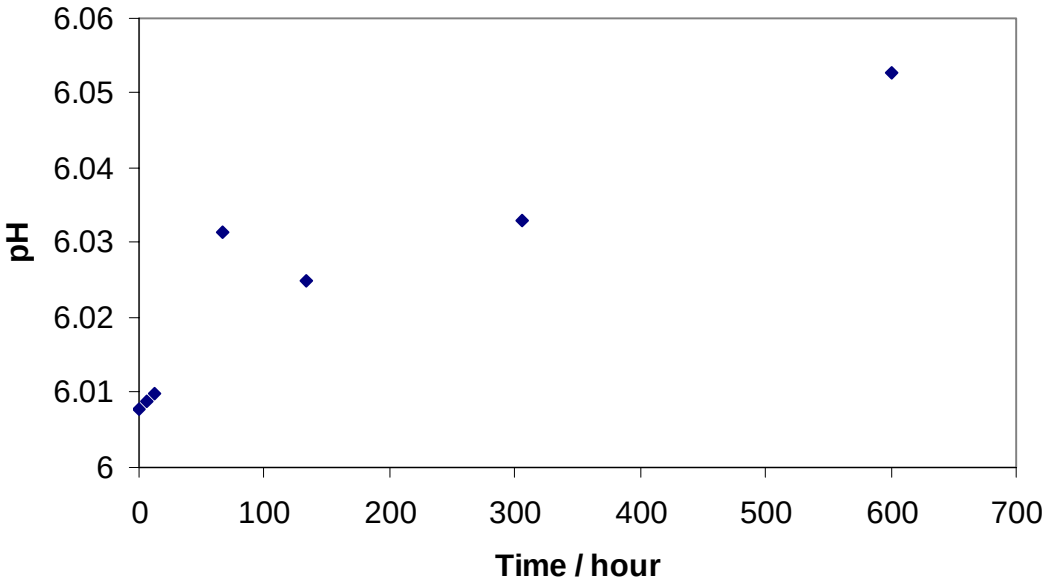

FIGURE 7. Predicted change of pH at the metal surface with respect to time at initial conditions of c_{H_2S} =120 ppm, T=60°C, P_{CO_2} = 7.7bar, pH 6.0, $c_{Fe^{2+}}$ =17 ppm, v=1 m/s.

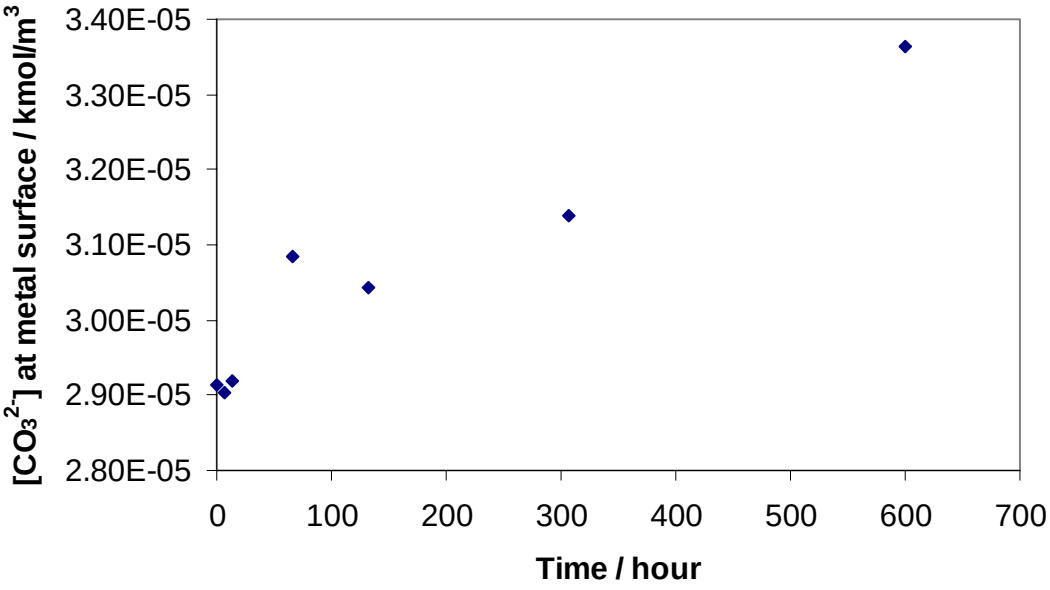

FIGURE 8. Predicted change of concentration of CO_3^{2+} at the metal surface with respect to time at initial conditions of c_{H_2S} =120 ppm, T=60°C, P_{CO_2} = 7.7bar, pH 6.0, $c_{Fe^{2+}}$ =17 ppm, v=1 m/s.

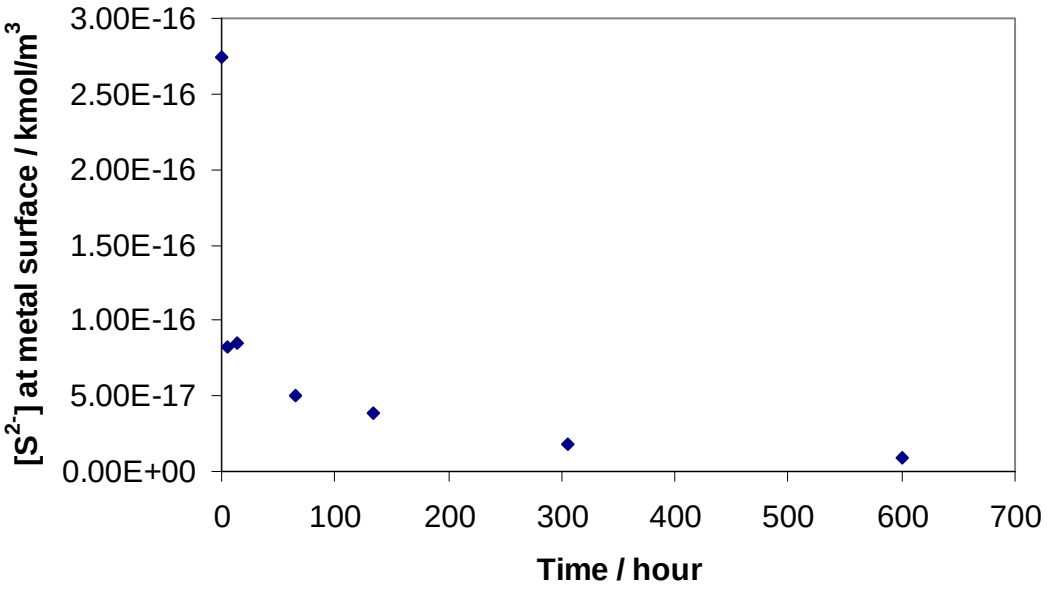

FIGURE 9. Predicted change of concentration of S^{2-} at the metal surface with respect to time at initial conditions of c_{H_2S} =120 ppm, T=60°C, P_{CO_2} = 7.7bar, pH 6.0, $c_{Fe^{2+}}$ =17 ppm, v=1 m/s.

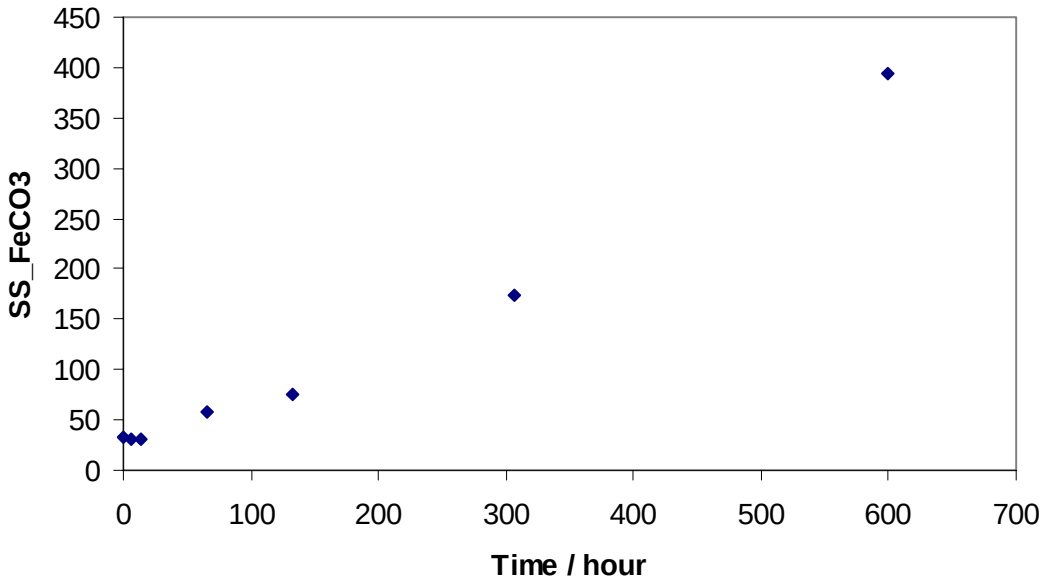

FIGURE 10. Predicted change $FeCO_3$ supersaturation at the metal surface with respect to time at initial conditions of c_{H_2S} =120 ppm, T=60°C, P_{CO_2} = 7.7bar, pH 6.0, $c_{Fe^{2+}}$ =17 ppm, v=1 m/s.

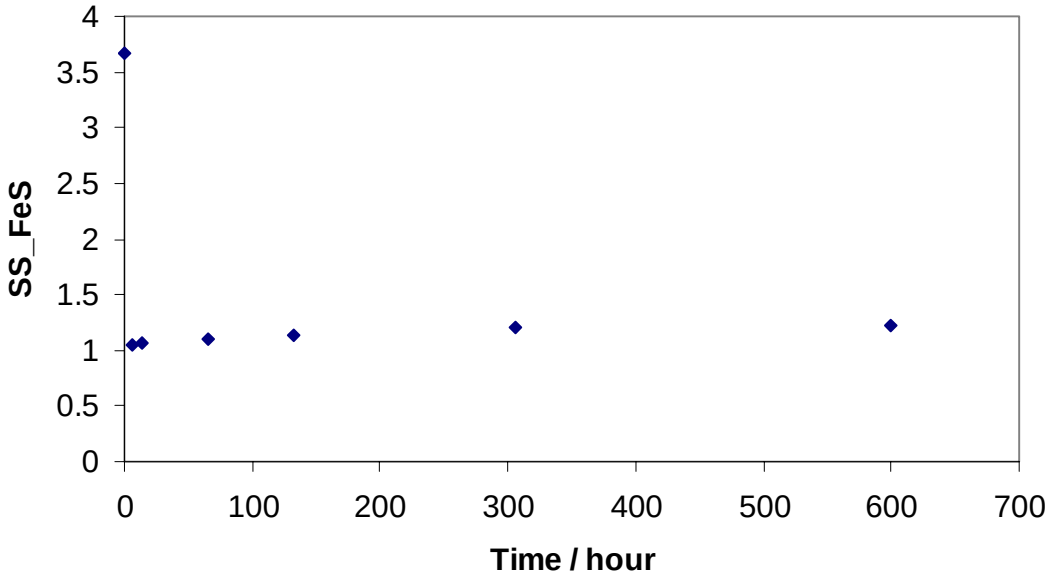

FIGURE 11. Predicted change FeS supersaturation at the metal surface with respect to time at initial conditions of c_{H_2S} =120 ppm, T=60°C, P_{CO_2} = 7.7bar, pH 6.0, $c_{Fe^{2+}}$ =17 ppm, v=1 m/s.

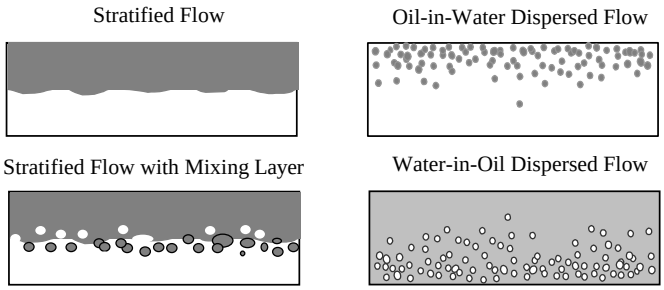

FIGURE 12. Flow patterns in oil-water horizontal flows

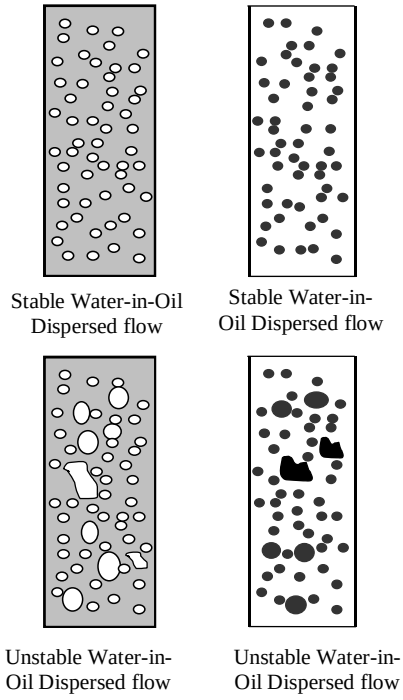

FIGURE 13. Flow patterns in oil-water upward and downward vertical flows

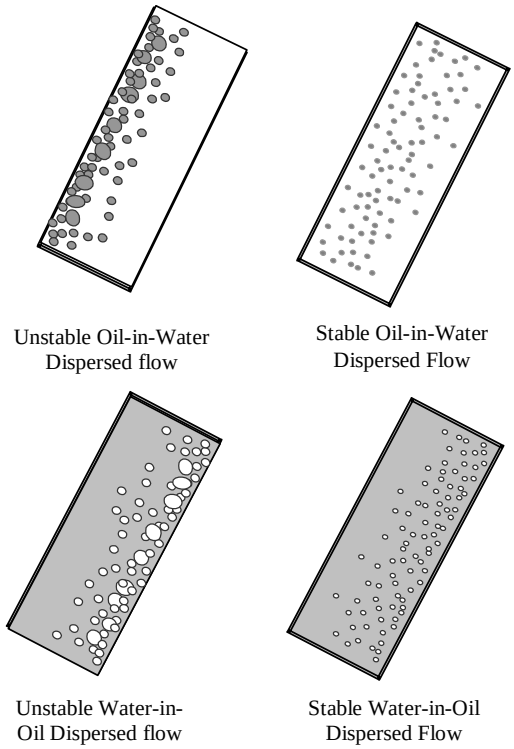

FIGURE 14. Flow patterns in oil-water upward inclined flows

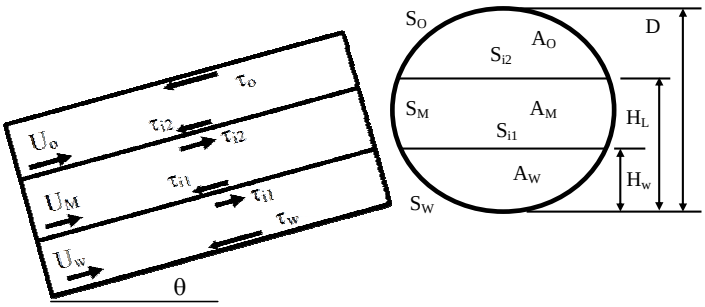

FIGURE 15. Schematic representation of the three-layer segregated oil-water flow

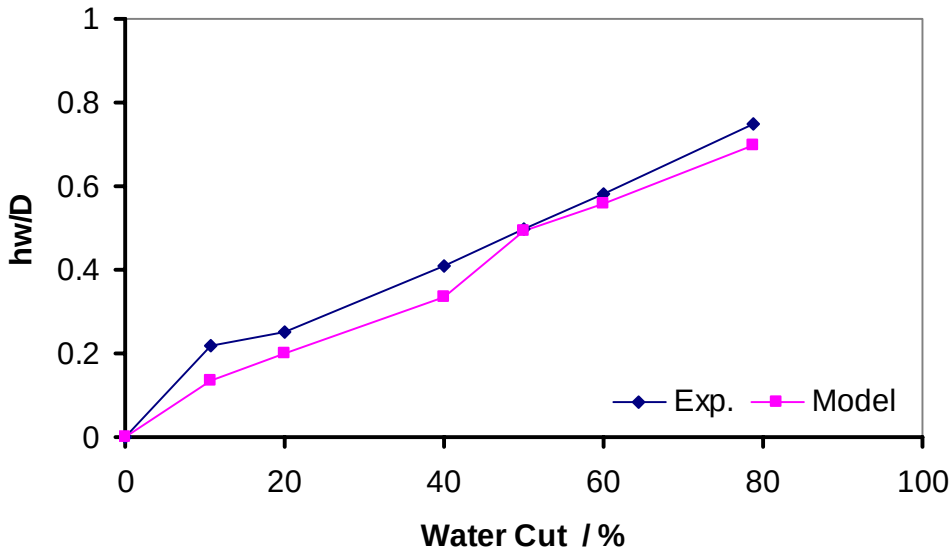

FIGURE 16. Comparison of water film height between experiments and the model predictions (0.45 m/s and horizontal)

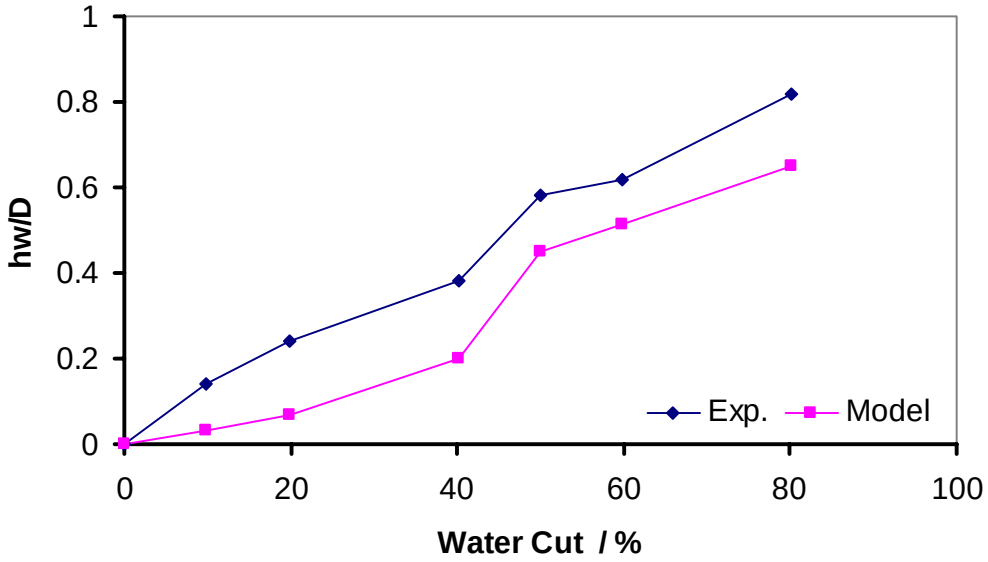

FIGURE 17. Comparison of water film height between experiments and the model predictions (1.80 m/s and horizontal).

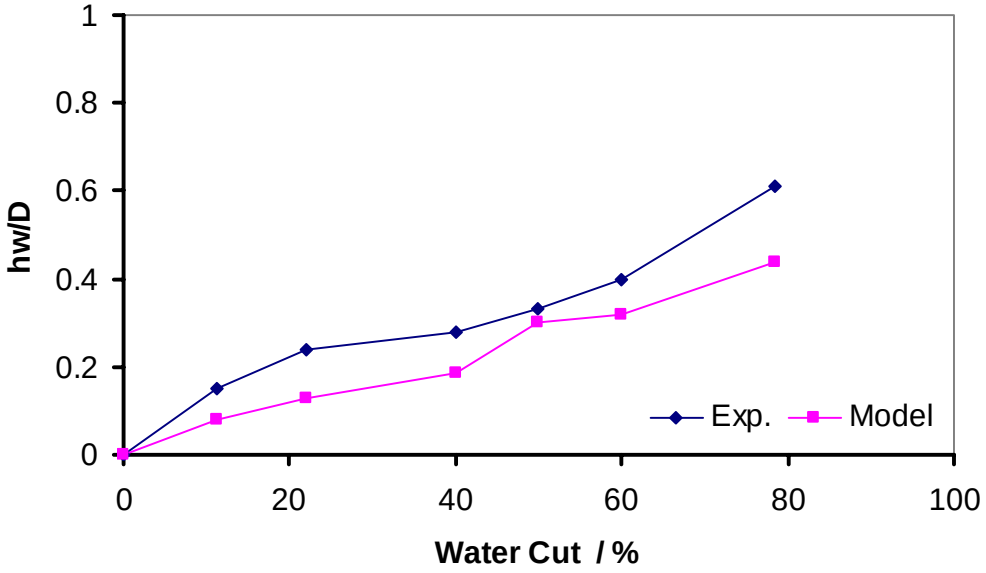

FIGURE 18. Comparison of water film height between experiments and the model predictions (0.45 m/s and -6 deg. downward inclined)

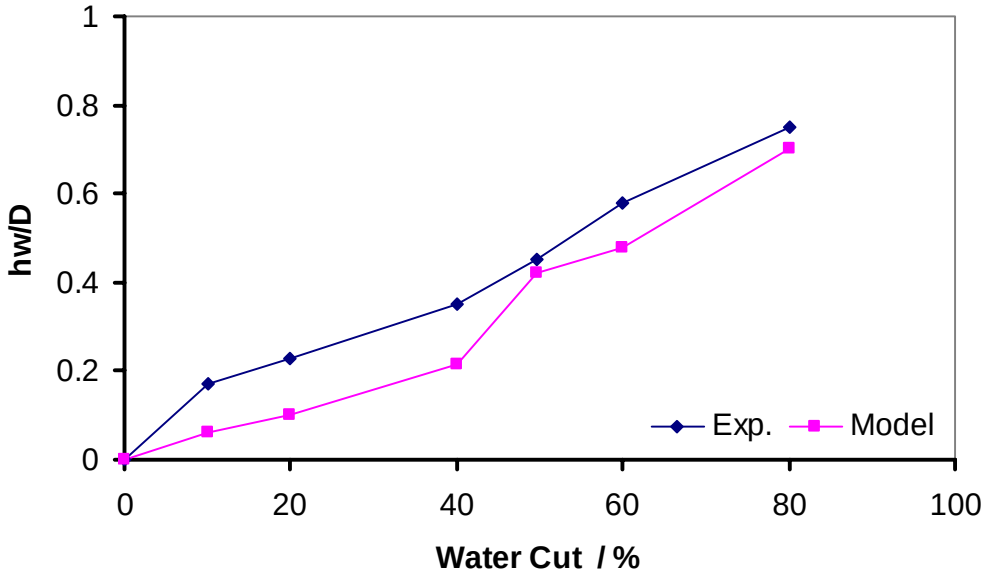

FIGURE 19. Comparison of water film height between experiments and the model predictions (1.35 m/s and -6 deg. downward inclined)

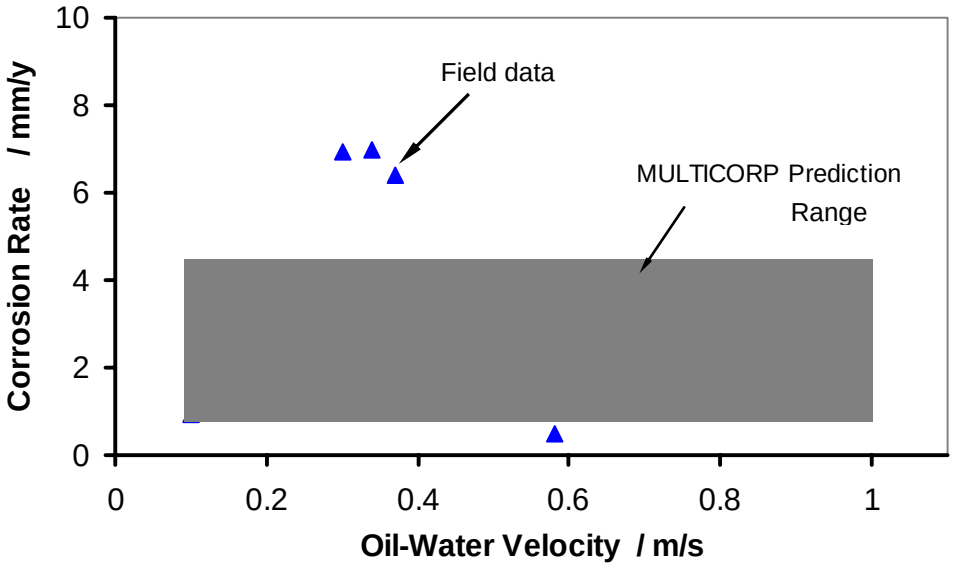

FIGURE 20. Comparison of corrosion rate between field data (Y. Gunaltun[51]) shown as points and the present model predictions shown as a hatched area denoting the range of values obtained by varying the input parameters as the precise values were not available.

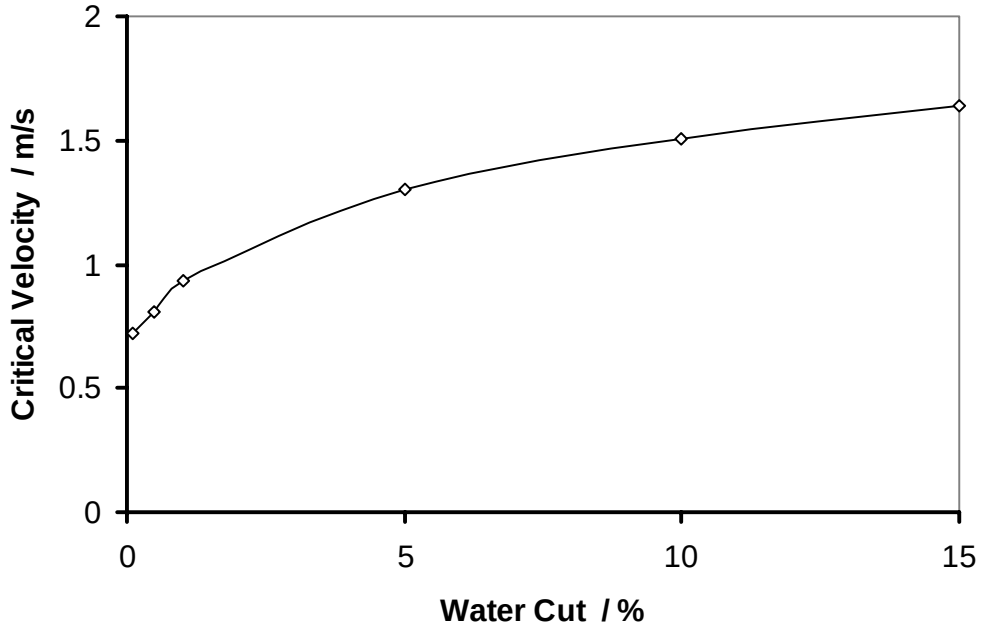

FIGURE 21. Effect of water cut on critical velocity for water entrainment at for an API=41 light oil, ρ_o=820 kg/m^3, μ_o=2 cP, d=0.1 m and σ=0.029 N/m

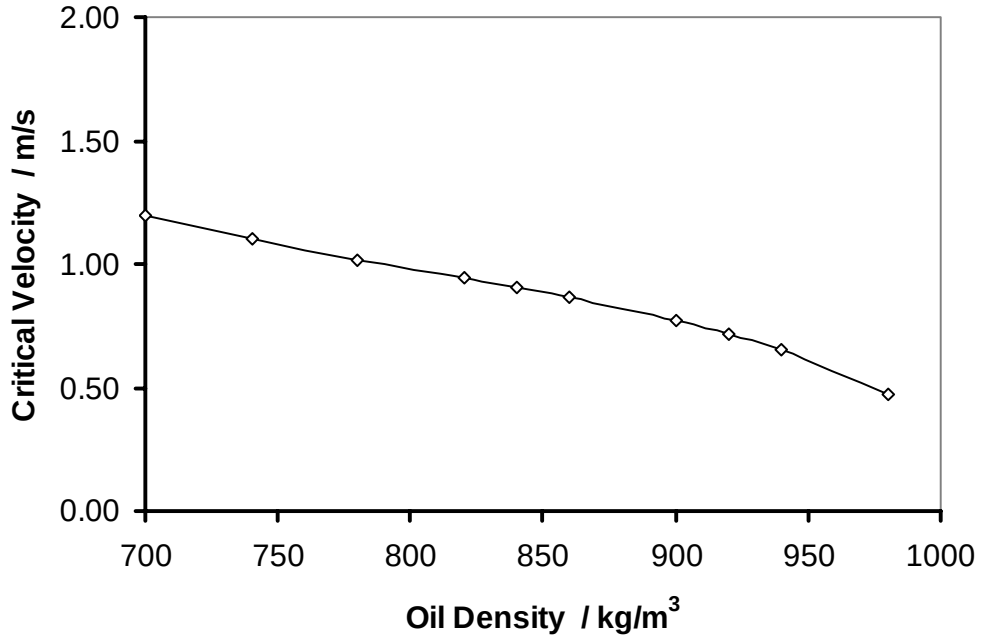

FIGURE 22. Effect of oil density on critical velocity at D=0.1 m, μ_o=2 cP, water cut=1% and σ=0.029 N/m

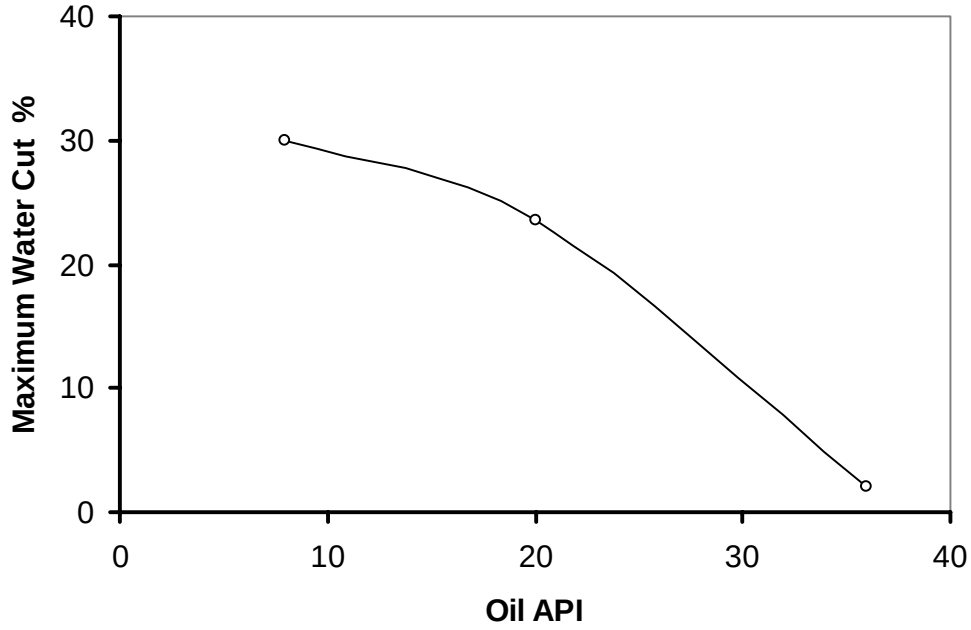

FIGURE 23. Effect of Oil API on the maximum water cut carried by the flowing oil phase at D=0.1 m, superficial oil velocity =1m/s, oil viscosity =2 ~ 70 cP in horizontal flow

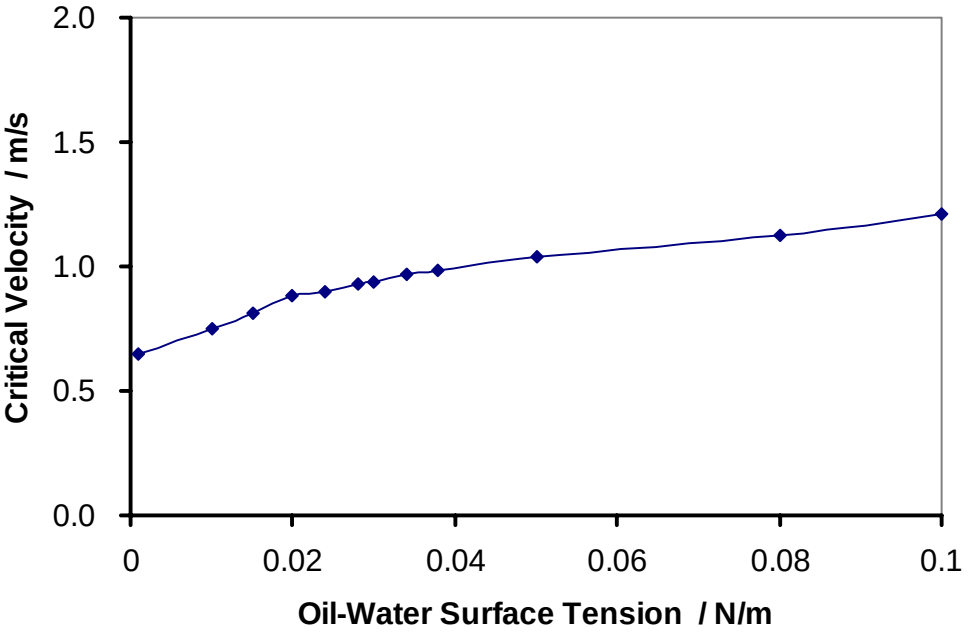

FIGURE 24. Effect of surface tension on critical velocity at D=0.1 m, μ_o=2 cP, water cut=1% and ρ_o=820 kg/m^3

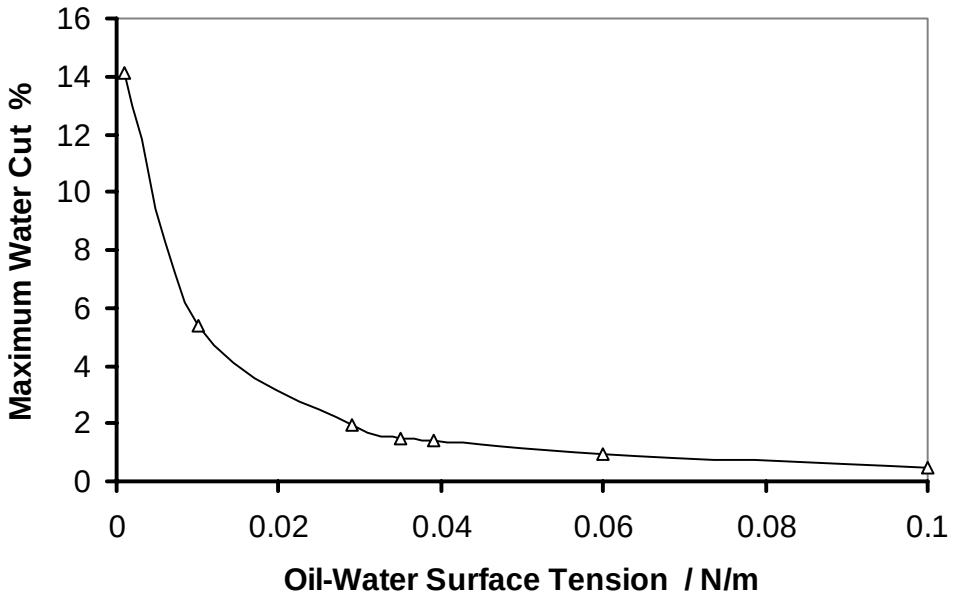

FIGURE 25. Effect of oil-water surface tension on the maximum water cut carried by the flowing oil phase at D= 0.1 m, superficial oil velocity =1m/s and API=36

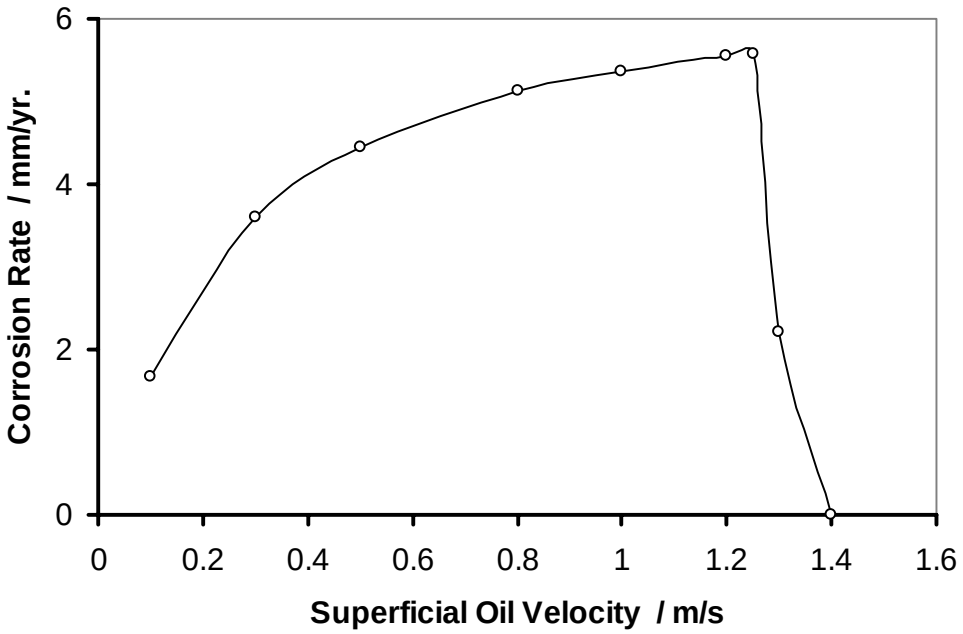

FIGURE 26. Relationship between corrosion rate and oil velocity at D= 0.1 m, water cut =5%, pH= 4 and oil API=45

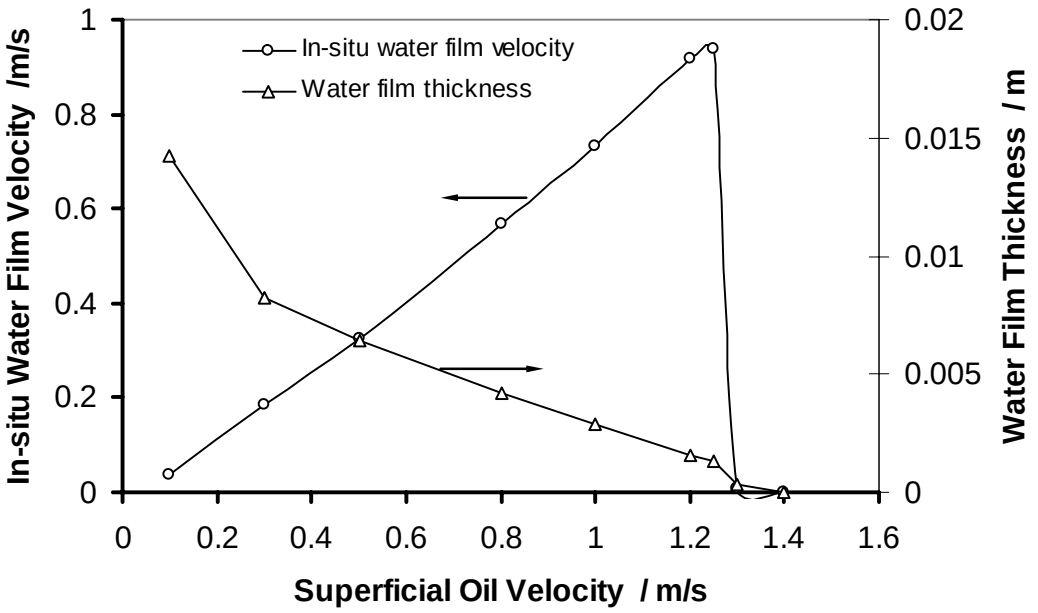

FIGURE 27. Changes of in-situ velocity and film thickness of water film along with superficial oil velocity at D= 0.1 m, water cut =5%, pH= 4 and oil API=45

TABLE 1. Experimental Test Matrix for CO_2/H_2S Corrosion in Scale-Free Conditions

Parameter	**Conditions**
CO_2 partial pressure	0.77MPa (7.7 bar)
Solution	1% NaCl solution, pH6
Corrosion Rate Measurement	Weight loss (C1018 and X-65) Linear Polarization Resistance
Single-phase flow	V_{sl} = 1 m/s
Temperature	60ºC
Test Time	25 days
H_2S gaseous concentration	120 ppm
Fe^{2+} concentration	17 ppm

TABLE 2 Summary of the experimental parameters
in the studies used for verification

Reference	D (cm)	ρ_o (kg/m^3)	ρ_w (kg/m^3)	μ_o (cP)	μ_w (cP)	σ (N/m)	θ (^{o})	T (°C)	ε_w (%)	V_m (m/s)
32	5.08	850	1000	29.6	1	0.036	0	20	10-90	0.5-3.0
34	5.08	856	1000	19~100	1	0.0335	90,75, 60, 45	32.2	3 ~95	0.1 ~ 2.5
36	5.9	790	1000	22-35	1	0.036	0	18-30	10-20	0.1-2.0
37	2.5-7.6	801	1000	1.6	1	0.017	0	20	20-80	0.7-3.9
48	10	820	1024	2	1	0.029	0	25	20-40	0.4-3.0
53	7.79	740	1000	0.7	0.5	0.032	-6 ~ 10	80	0 ~ 80	0.45 ~ 1.8

NOTE					
D	Pipe diameter		σ	Oil-water surface tension	
ρ_o	Oil density		θ	Pipe inclination	
ρ_w	Water density		T	temperature	
μ_o	Oil viscosity		ε_w	Water cut	
μ_w	Water viscosity		V_m	Oil-water mixture velocity	

TABLE 3 Umm Al Dakh Field Well Data (Gunaltun[51])

	Umm Al Dalkh
WHFP (bars)	20 ~75
WHFT (^{o}C)	30 ~ 70
BHFP (bars)	235 ~260
BHFT (^{o}C)	100
Oil production rate (bopd)	65 ~ 2100
Water cut (%)	Up to 70
Oil density (at 20 ^{o}C)	0.872
CO2 content of the well fluid (mole %)	2.5
H2S content of the well fluid (mole %)	nil
GOR (SCF/SB)	70 ~ 200
Gas molar weight	
Tubing size (inch)	2 3/8 ~ 3 ½
Tubing material	C-75
Deviation (degree)	Up to 40
Water composition (mg/l)	
Na^{+}	59525
Ca^{++}	5890
Mg^{++}	755
K^{+}	270
Fe^{++}	
Ba^{++}	
Sr^{++}	770
Cl^{-}	104425
HCO_3^{-}	410
SO_4^{--}	260
pH (20 ^{o}C)	7.2